J. Fluid Mech. (1994), *vol.* 266, *pp.* 209–242

Bifurcation and chaos in shape and volume oscillations of a periodically driven bubble with two-to-one internal resonance

By Z. C. FENG† AND L. G. LEAL

Department of Chemical and Nuclear Engineering, University of California at Santa Barbara,
Santa Barbara, CA 93106, USA

(Received 16 November 1992 and in revised form 18 August 1993)

We study the dynamic sof gas or vapour bubbles when the volume mode of oscillation is coupled with one of the shape modes through quadratic resonance. In particular, the frequency ratio of the volume mode and the shape mode is assumed to be close to two-to-one. The analysis is based upon the use of a two-timescale asymptotic approximation, combined with domain perturbation theory. The viscous effect of the fluid is included by using a rigorous treatment of weak viscosity. Through solvability conditions, amplitude equations governing the slow-timescale dynamics of the resonant modes are obtained. Bifurcation analysis of these amplitude equations reveals interesting phenomena. When volume oscillations are forced by oscillations of the external pressure, we find that the volume mode may lose stability for sufficiently large amplitudes of oscillation, and this instability may lead to chaotic oscillations of both the volume and the shape modes. However, we find that for chaos to occur, a critical degree of detuning is required between the shape and volume modes, in the sense that their natural frequencies must differ by more than a critical value. When a shape mode is forced by oscillations of anisotropic components of the external pressure, we find that chaos can occur even for exact resonance of the two modes. The physical significance of this result is also given.

1. Introduction

The dynamics of a single spherical bubble forced by a periodic pressure field has been studied extensively. The review article of Plesset & Prosperetti (1977) describes the literature up to the mid-1970s. Recently, the primary research focus has been on nonlinear aspects of the bubble motion including, in particular, the existence of chaotic oscillations of bubble volume. The work on this suject can be conveniently divided into two classes according to whether the bubble is composed of gas or vapour (the difference lies in the fact that the volume of a vapour bubble can become unbounded for sufficiently large initial spherical perturbations from the equilibrium radius). For a gas bubble, Lauterborn & Parlitz (1988), Smereka, Birnir & Banerjee (1987), and Parlitz *et al.* (1990) have shown that a single spherical bubble under isotropic periodic pressure variations can oscillate chaotically leading to dynamics on a strange attractor. For a vapour bubble, Szeri & Leal (1991) have used a generalized Melnikov theory due to Wiggins (1988) to calculate threshold values of the forcing amplitude for the onset of chaotic oscillations which occur via the breakup of the homoclinic orbits. They have

---

† Present address: Department of Mechanical Engineering, Massachusetts Institute of Technology, Cambridge, MA 02139, USA.

found that the threshold values depend on the complexity of the forcing function; namely, the presence of two or more forcing frequencies lowers the critical amplitude of the pressure perturbations, relative to that required for a single-frequency oscillation.

Many predictions concerning regular motions in the nonlinear regime for a single bubble in a time-varying pressure field have been reproduced in experiments reported by Crum & Prosperetti (1983). However, the chaotic oscillations predicted in the above numerical and theoretical work have not been seen. Attempts to achieve chaotic oscillation of bubble volume (radius) have apparently been thwarted by the onset of noticeable shape oscillations, see Holt & Crum (1992). Since all of the numerical as well as analytic works cited above are based on the assumption that the bubble remains spherical, a new theory which includes the coupling between shape and volume oscillations is required to understand chaotic dynamics of a single bubble as seen in experiments.

Chaotic bubble oscillations, when one (or more) shape modes is coupled with the volume mode, can also provide at least one explanation for interesting new physical phenomena. Among them is the erratic position of a bubble in a sound field (called dancing) when the amplitude of the sound exceeds a certain threshold (Strasberg & Benjamin 1958; Benjamin & Ellis 1990). Other phenomena, to be examined later in this paper, are associated with large-amplitude shape oscillations when chaos arises. In these circumstances, the amplitude of the shape oscillations will be time dependent and the peak amplitude of the shape mode can be much larger than the time-averaged amplitude. Large-amplitude shape oscillation implies large shear stresses near the surface of the bubble, which may be very important in certain applications. For example, large shear stresses can be the cause of damage in biological systems exposed to ultrasound (Young 1989, chap. 3).

In this paper, we study the bubble dynamics when the breathing mode is coupled with one of the shape modes through *quadratic* resonance, which occurs when the frequency ratio of the breathing mode to the shape mode is two to one. This relationship between the frequency of the breathing mode and the frequency for any one of the possible shape modes is satisfied for a specific bubble size. Although resonant interactions are also possible for a number of other conditions of frequency matching, the two-to-one resonant condition corresponds to the fastest energy transfer between the modes; see Yang, Feng & Leal (1993). For this reason, we postpone to a later paper any study of the weaker and slower resonant combinations that occur under other resonant conditions. Additional discussion of the motivation for studying the two-to-one internal resonance is contained in Longuet-Higgins (1989). We study two types of pressure forcing. First, we study isotropic forcing, where the breathing mode is excited by nearly resonant forcing and one of the shape modes obtains energy through resonant interaction with the breathing mode. Second, we study anisotropic forcing (corresponding to a position-dependent pressure at the bubble surface), where one of the shape modes is excited by nearly resonant pressure oscillations and the breathing mode obtains energy through nonlinear coupling.

Part of the objective of this paper is to present a comprehensive picture of the several bifurcation sequences that are possible. We achieve this objective by presenting bifurcation sets, where the system parameter space, such as the forcing frequency and amplitude, is divided into a finite number of sets, inside which the qualitative behaviour of the system is the same. We also present bifurcation diagrams, which demonstrate how the qualitative behaviour changes as one of the system parameters is changed while the rest remain fixed.

There are two prior studies that are closely related to the problem to be studied here.

First, is the work of Mei & Zhou (1991) who studied the resonant interaction between a spherical (pure volume) oscillation and one or two distortional modes for a bubble in water when the spherical mode is forced by ambient sound, i.e. by periodic oscillation of an isotropic pressure field. They have found numerical evidence of chaotic bubble oscillations. Mei & Zhou suggested that this result, combined with the theory of Benjamin & Ellis (1990), provided one mechanism to explain the erratic dancing of a bubble in sound. Since Mei & Zhou were mainly interested in providing a phenomenological explanation for the erratic dancing phenomenon, the bifurcation sequence that leads to chaotic motion was not explored. However, knowledge of the bifurcation sequence will be crucial in any attempt to corroborate theory with laboratory experiments. Further, we shall see that the bubble response is quite different when the pressure forcing is anisotropic instead of isotropic as considered by Mei & Zhou.

The second related work is our own recent publication, Feng & Leal (1993), on the oscillation of an initially perturbed bubble in an inviscid fluid, but without time-dependent pressure forcing. In that paper, we considered both one-to-one and two-to-one internal resonance conditions between the radial (or volume) mode and one of the distortion modes. In the latter case, it was shown that when the initial amplitude of the radial deformation exceeds a threshold value (that depends upon the proximity to exact resonance) a homoclinic orbit appears (in a reduced two-dimensional description of the modal amplitude dynamics) which emanates from the fixed point that corresponds to purely radial oscillations. It is thus clear that the addition of a periodic pressure perturbation of any amplitude to this inviscid system will produce chaotic dynamics in at least the vicinity of the unperturbed homoclinic orbit. Further, if a very weak damping is added, of $O(\epsilon^n)$ for $n > 1$ (where the amplitude of the bubble deformation is $O(\epsilon)$), chaotic dynamics will still be realized if the amplitude of the forcing is large enough. However, if the viscous damping is any larger, it is impossible to anticipate the dynamic response to periodic forcing (cf. Kovacic & Wiggins 1992), and it is this latter, more difficult, class of problems that we consider here, via the special case in which the damping is $O(\epsilon)$ and the forcing of $O(\epsilon^2)$.

The paper is organized as follows. In §2, we combine the asymptotic method of domain perturbations with a multiple-timescale analysis (cf. Nayfeh & Mook 1979) to derive governing equations and boundary conditions for bubble deformation at successive orders in the amplitudes of shape and volume modes In §3, solvability conditions are used to obtain governing equations for the slowly varying amplitude functions that occur at resonance. In §4 we show that the amplitude equations for the shape mode can be generalized to include forcings whose frequency is away from the resonance. In §§5 and 6, bubble dynamics under isotropic and anisotropic forcing are studied separately. A discussion of the physical consequences of the participation of shape modes in bubble oscillations due to isotropic pressure fluctuations is given in §7.

2. Formulation of the problem

Our problem formulation is closely related to that in Yang *et al.* (1993). We modify that formulation, however, to include weak viscous effects.

Consider a bubble of radius a in the quiescent state. Characteristic scales for length l_c, time t_c, and pressure p_c are then identified as a, $(a^3\rho/\Gamma)^{\frac{1}{2}}$, and Γ/a, respectively, where Γ is the surface tension and ρ the density of the liquid. The viscosity of the liquid is said to be weak if the parameters $S = t_c/(a^2/\nu)$ is small. For air bubbles in water with radius between 0.01 and 1.00 cm, taking $\Gamma = 75$ dyne cm^{-1}, $\rho = 1$ g cm^{-3}, $\nu = 0.013$ cm^2 s^{-1},

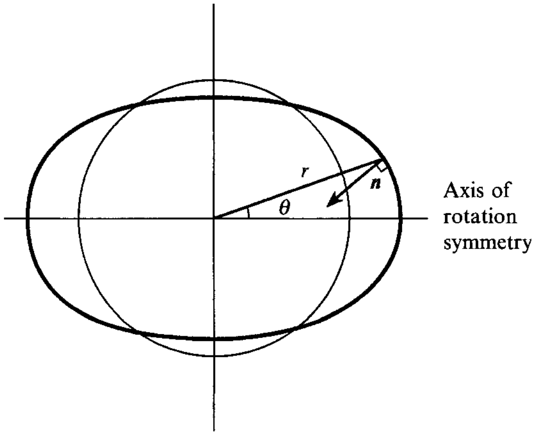

FIGURE 1. The coordinate system that describes the bubble geometry.

we have S lying between 0.015 and 0.00015. We can thus assume $S \ll 1$. (For small bubbles, however, other mechanisms of energy dissipation may dominate that due to viscous effects, see Longuet-Higgins 1989.) This assumption, combined with the assumption that the deformation of the bubble from its equilibrium spherical shape is small, allows us to approximate the motion as potential flow with a thin boundary layer near the surface of the bubble. Thus if we denote the non-dimensionalized velocity potential for the liquid as ϕ, and specify the non-dimensionalized bubble deformation via the function f, i.e. $F = r-1-f(\phi, t) = 0$ in spherical coordinates (see figure 1), we have the equation governing the liquid motion:

$$\nabla^2\phi = 0 \quad \text{for} \quad r > 1+f(\theta, t), \tag{1}$$

and on the bubble surface we have the kinematic boundary condition:

$$\frac{\partial F}{\partial t} + \nabla\phi \cdot \nabla F = 0. \tag{2}$$

Kang & Leal (1988) have utilized an analysis similar to that of Prosperetti (1977) to conclude that weak viscous effects in the boundary layer are equivalent to a modification of the dynamic boundary condition. The normal stress condition, with the pressure correction and viscous stress terms included is

$$-p_v + \left(\tilde{P} - P_0 + \frac{\partial \phi}{\partial t} + \tfrac{1}{2}\nabla\phi \cdot \nabla\phi\right) + 2S\frac{\partial^2 \phi}{\partial n'^2} = A(\theta, t) + \nabla \cdot \boldsymbol{n}, \tag{3}$$

where P_0 denotes the non-dimensionalized pressure at infinity; $\tilde{P}$ denotes the pressure inside the bubble; p_v is the pressure correction, which will be explained in a moment; and $\partial/\partial n'$ denotes differentiation in the direction of the outward normal vector.

We call attention to the term $A(\theta, t)$ in the normal stress condition (3). This represents an imposed time- and spatially dependent pressure at the bubble surface. This type of surface pressure is often called the radiation pressure. In experiments, spatially and time-dependent radiation pressure can be produced via the superposition of two ultrasonic acoustic wave fields with slightly different frequencies, see Marston & Apfel (1980). We restrict the analysis to axisymmetric surface pressure distributions in this paper. Specifically we consider two cases. In the first, which will hereafter be referred to as the isotropically forced case, we consider the surface pressure to be a time-periodic function but independent of θ. In the second case, which will hereafter be referred as the anisotropically forced case, we consider the surface pressure to be a time-periodic function but dependent on θ. In order to facilitate the problem formulation, we shall let

$$A(\theta, t) = A_0 \cos 2\Omega t + A_n \cos \Omega t P_n(\cos\theta), \tag{4}$$

where $P_n(\cos\theta)$ is the Legendre polynomial of $\cos\theta$. Since we consider the two cases ($A_0 \neq 0$ and $A_n \neq 0$) separately, there is no need to allow a phase separation between the two forcing functions. It should be noted that the characteristic frequency Ω is non-dimensionalized (scaled) with respect to the characteristic timescale $(a^3\Gamma/\rho)^{\frac{1}{2}}$.

The viscous pressure correction p_v can be calculated when the parameter S is small and the deformation of the bubble from the spherical shape is also small. In that case, Kang & Leal have obtained

$$p_v = S \sum_{m=0}^{\infty} T_m P_m(\cos\theta), \tag{5}$$

where T_m is determined from the shear stress condition on the bubble surface,

$$-\sum_{m=0}^{\infty} m T_m \frac{\mathrm{d}P_m(\cos\theta)}{\mathrm{d}\theta} = 2\left[\frac{\partial\phi}{\partial\theta} - \frac{\partial^2\phi}{\partial r\,\partial\theta}\right]. \tag{6}$$

The pressure inside the bubble $\tilde{P}$ depends on the gas content of the bubble. In this paper, we consider both a gas bubble and an isothermal vapour bubble (by a vapour bubble, we mean a bubble that has partial pressure due to the vapour content). For a gas bubble, the pressure inside the bubble is assumed to obey the perfect gas law

$$\tilde{P} = \tilde{P}_0 \langle (1+f)^3 \rangle^{-\gamma}, \tag{7}$$

in which $\langle \cdot \rangle$ denotes the spherical surface average. For axisymmetric problems

$$\langle g(\theta) \rangle = \frac{1}{2}\int_0^{\pi} g(\theta) \sin\theta \,(\mathrm{d}\theta),$$

$\tilde{P}_0$ is the equilibrium pressure for a spherical bubble, (i.e. $\tilde{P}_0 - P_0 = 2$), and γ is the ratio of the specific heats. For an isothermal vapour bubble, the pressure inside the bubble can be assumed to be

$$\tilde{P} = \tilde{P}_g \langle (1+f)^3 \rangle^{-1} + \tilde{P}_v, \tag{8}$$

where $\tilde{P}_g$ and $\tilde{P}_v$ are the partial pressures inside the bubble at the quiescent state due to the gas and the vapour respectively. Both are constants for isothermal processes.

For f small, the method of 'domain perturbations' can be used to express the boundary conditions on the deformed bubble surface in terms of asymptotically equivalent boundary conditions on the undeformed surface, $r = 1$; see Joseph (1973). With the above assumptions and definitions, the kinematic boundary condition at $r = 1$ is

$$\frac{\partial f}{\partial t} - \frac{\partial\phi}{\partial r} = f\frac{\partial^2\phi}{\partial r^2} - (1-\eta^2)\left\{\frac{\partial f}{\partial\eta}\frac{\partial\phi}{\partial\eta} - 2f\frac{\partial f}{\partial\eta}\frac{\partial\phi}{\partial\eta} + f\frac{\partial f}{\partial\eta}\frac{\partial^2\phi}{\partial r\,\partial\eta}\right\} + \frac{f^2}{2}\frac{\partial^3\phi}{\partial r^3} + O(f^3)$$

and the normal stress condition is

$$\begin{aligned}\frac{\partial\phi}{\partial t} + (\nabla_s^2+2)f - (\omega_0^2+2)\langle f \rangle &= A(\theta,t) - f\frac{\partial^2\phi}{\partial t\,\partial r} - \tfrac{1}{2}(\nabla\phi)^2 + 2f(f+\nabla_s^2 f)\\ &\quad + (\omega_0^2+2)\{\langle f^2\rangle - \tfrac{3}{2}(1+\gamma)\langle f\rangle^2\} - \frac{f^2}{2}\frac{\partial^3\phi}{\partial t\,\partial r^2} - \frac{f}{2}\frac{\partial}{\partial r}(\nabla\phi\cdot\nabla\phi) - \frac{f^2}{6}\frac{\partial^2}{\partial r^2}(\nabla\phi\cdot\nabla\phi)\\ &\quad - 2S\frac{\partial^2\phi}{\partial r^2} + S\sum_{m=0}^{\infty} m T_m P_m(\cos\theta) + O(f^3),\end{aligned}$$

where $$\nabla_s^2 = \frac{\partial}{\partial\eta}\left\{(1-\eta^2)\frac{\partial}{\partial\eta}\right\}, \qquad \eta = \cos\phi,$$

and $\omega_0^2 = 3\gamma(P_0+2)-2$ for an ideal gas bubble, $\omega_0^2 = 3(P_0-\tilde{P}_v+2)-2$ for an isothermal vapour bubble.

For convenience of treating near-resonant cases, we introduce an additional scaling of ϕ and t,

$$\tilde{t} = \Omega t, \quad \tilde{\phi} = \phi/\Omega$$

to obtain $$\nabla^2\tilde{\phi} = 0 \tag{9}$$

and the boundary conditions at $r = 1$

$$\frac{\partial f}{\partial \tilde{t}} - \frac{\partial\tilde{\phi}}{\partial r} = f\frac{\partial^2\tilde{\phi}}{\partial r^2} - (1-\eta^2)\frac{\partial f}{\partial\eta}\frac{\partial\tilde{\phi}}{\partial\eta} + \text{Higher-order terms,} \tag{10}$$

$$\begin{aligned}\Omega^2\frac{\partial\tilde{\phi}}{\partial\tilde{t}} + (\nabla_s^2+2)f - (\omega_0^2+2)\langle f\rangle &= A(\theta,t) - \Omega^2 f\frac{\partial^2\tilde{\phi}}{\partial\tilde{t}\,\partial r} - \tfrac{1}{2}\Omega^2(\nabla\tilde{\phi})^2 + 2f(f+\nabla_s^2 f)\\ &+ (4\omega_0^2+2)\{\langle f^2\rangle - \tfrac{3}{2}(1+\gamma)\langle f\rangle^2\} - 2S\Omega\frac{\partial^2\tilde{\phi}}{\partial r^2} + S\sum_{m=0}^{\infty} mT_m P_m(\eta) + \text{Higher-order terms.}\end{aligned} \tag{11}$$

In summary then, the problem is to solve the differential equation (9) subject to the conditions (10) and (11).

The analysis that follows is based upon the use of an asymptotic approximation of the solution for a small parameter ϵ. Since we limit our consideration to conditions of quadratic resonance (or near resonance) between shape and volume modes and/or resonance between the oscillatory modes and the forcing $A(\theta, t)$, it is convenient to anticipate from the outset that resonant interactions will occur on a much longer timescale than that associated with the forcing, and introduce a second 'independent' timescale τ as defined below. Thus, the shape function f and the velocity potential ϕ are expanded in the forms

$$r = 1+f = 1+\epsilon f_1(\tilde{t},\tau,\eta)+\epsilon^2 f_2(\tilde{t},\tau,\eta)+\dots, \tag{12}$$

$$\tilde{\phi} = \epsilon\phi_1(\tilde{t},\tau,\eta,r)+\epsilon^2\phi_2(\tilde{t},\tau,\eta,r)+\dots, \tag{13}$$

where $$\tau = \epsilon t \tag{14}$$

is the slow timescale characteristic of the resonant interaction between shape and volume modes (we express τ in terms of the original dimensionless time t so that the time-like variable $\tilde{t}$ will not be used in later analysis). As stated above, the present analysis is focused on the condition in which the natural frequency for oscillation of the nth shape mode is approximately one-half the natural frequency for purely radial volume oscillation, so that resonant interactions occur at $O(\epsilon^2)$. In particular, we allow for an $O(\epsilon)$ mismatch between the natural frequencies of the purely radial and shape modes of bubble oscillation, so that

$$\omega_0 = 2\omega_n + \epsilon\beta_0, \tag{15}$$

where $\omega_n^2 = (n-1)(n+1)(n+2)$. In addition, we consider the forcing frequency for anisotropic pressure oscillations to be

$$\Omega = \omega_n + \epsilon\sigma_n. \tag{16}$$

Taken together, the conditions (15) and (16) also imply that the forcing frequency for isotropic pressure fluctuations (2Ω) is within $O(\epsilon)$ of the natural frequency of the volume mode (ω_0). Since we are forcing the bubble to oscillate near its resonance frequency, we assume that the forcing amplitudes

$$A_0 = \epsilon^2 \tilde{A}_0, \quad A_n = \epsilon^2 \tilde{A}_n \tag{17}$$

are of second order in ϵ so that the shape deformation is no larger than first order. Restricting our analysis to a weakly viscous fluid, we further assume

$$S = \epsilon \tilde{S} \tag{18}$$

and

$$T_m = \epsilon T_{1m} + \epsilon^2 T_{2m} + \dots. \tag{19}$$

Substituting (12)–(19) into (9), (10) and (11), we obtain at $O(\epsilon)$:

$$\nabla^2 \phi_1 = 0, \tag{20}$$

with the boundary conditions at $r = 1$

$$\frac{\partial f_1}{\partial \tilde{t}} - \frac{\partial \phi_1}{\partial r} = 0 \tag{21}$$

$$\omega_n^2 \frac{\partial \phi_1}{\partial \tilde{t}} + (\nabla_s^2 + 2) f_1 - (4\omega_n^2 + 2) \langle f_1 \rangle = 0. \tag{22}$$

At $O(\epsilon^2)$, we obtain

$$\nabla^2 \phi_2 = 0, \tag{23}$$

with the boundary conditions at $r = 1$

$$\frac{\partial f_2}{\partial \tilde{t}} - \frac{\partial \phi_2}{\partial r} = -\frac{1}{\omega_n} \frac{\partial f_1}{\partial \tau} + f \frac{\partial^2 \phi_1}{\partial r^2} - (1 - \eta^2) \frac{\partial f_1}{\partial \eta} \frac{\partial \phi_1}{\partial \eta}, \tag{24}$$

$$\begin{aligned} \omega_n^2 \frac{\partial \phi_2}{\partial \tilde{t}} + (\nabla_s^2 + 2) f_2 - (4\omega_n^2 + 2) \langle f_2 \rangle &= -\omega_n \frac{\partial \phi_1}{\partial \tau} + 4\omega_n \beta_0 \langle f_1 \rangle - 2\omega_n \sigma_n \frac{\partial \phi_1}{\partial \tilde{t}} \\ &\quad + \tilde{A}_0 \cos 2\tilde{t} + \tilde{A}_n \cos \tilde{t} P_n(\eta) - \omega_n^2 f \frac{\partial^2 \phi_1}{\partial \tilde{t}\, \partial r} - \tfrac{1}{2}\omega_n^2 (\boldsymbol{\nabla} \phi_1)^2 + 2 f_1 (f_1 + \nabla_s^2 f_1) \\ &\quad + (\omega_n^2 + 2)\{\langle f_1^2 \rangle - \tfrac{3}{2}(1+\gamma) \langle f_1 \rangle^2\} - 2\tilde{S} \omega_n \frac{\partial^2 \phi_1}{\partial r^2} + \tilde{S} \sum_{m=0}^{\infty} m T_{1m} P_m(\eta). \end{aligned} \tag{25}$$

The term T_{1m} can be determined by substituting (19) and (13) into (6) to get

$$-\sum_{m=0}^{\infty} T_{1m} \frac{\partial P_m}{\partial \theta} = 2 \left[\frac{\partial \phi_1}{\partial \theta} - \frac{\partial^2 \phi_1}{\partial r\, \partial \theta} \right]. \tag{26}$$

In the analysis that follows, we solve the hierarchy of equations (20)–(26) to study the bubble response to either an isotropic or an anisotropic pressure oscillation.

A general solution of the governing equation at $O(\epsilon)$ is easily obtained by separation of variables:

$$f_1 = \frac{1}{2} \sum_{k=0}^{\infty} a_k \exp\left(\frac{\mathrm{i}\omega_k \tilde{t}}{\omega_n}\right) P_k(\eta) + \text{c.c.},$$

$$\phi_1 = -\frac{\mathrm{i}}{2} \sum_{k=0}^{\infty} \frac{a_k \omega_k}{(k+1)\,\omega_n\, r^{k+1}} \exp\left(\frac{\mathrm{i}\omega_k \tilde{t}}{\omega_n}\right) P_k(\eta) + \text{c.c.}$$

The occurrence of ω_n is due to the peculiar choice of the timescale. Here, $k = 0$ corresponds to the volume mode and $k \geqslant 2$ correspond to the shape modes ($k = 1$ corresponds to translation of the bubble and will hence be excluded from our analysis). Although the general solution allows for all possible modes (excluding $k = 1$), the fact that the system is damped at $O(\epsilon)$, and is forced with pressure fluctuations that are only $O(\epsilon^2)$ in amplitude, means that it is only the two modes that are in quadratic resonance with each other, and with the forcing, that will be present at $O(\epsilon)$. Hence, without loss of generality we let

$$f_1 = \tfrac{1}{2}\{\alpha_{1,0}(\tau)\,\mathrm{e}^{2\mathrm{i}\tilde{t}} + \alpha_{1,n}(\tau)\,\mathrm{e}^{\mathrm{i}\tilde{t}} P_n(\eta)\} + \text{c.c.}, \tag{27}$$

$$\phi_1 = -\mathrm{i}\left[\frac{1}{r}\alpha_{1,0}(\tau)\,\mathrm{e}^{2\mathrm{i}\tilde{t}} + \frac{1}{2(n+1)\,r^{n+1}}\alpha_{1,n}(\tau)\,\mathrm{e}^{\mathrm{i}\tilde{t}} P_n(\eta)\right] + \text{c.c.}, \tag{28}$$

where c.c. denotes complex conjugates of the preceding terms. It is obvious that these functional forms satisfy the governing equation (20) as well as the boundary conditions (21) and (22) at $O(\epsilon)$.

The problem at $O(\epsilon^2)$ can now be approached using the solutions (27) and (28) at $O(\epsilon)$. Specifically, by substituting (28) into (26), we obtain

$$\left.\begin{aligned} T_{1m} &= 0 \quad \text{for} \quad m \neq n, \\ T_{1m} &= \frac{n+2}{n+1}\mathrm{i}\omega_n\,\alpha_{1,n}\,\mathrm{e}^{\mathrm{i}\tilde{t}} + \text{c.c.} \quad \text{for} \quad m = n. \end{aligned}\right\} \tag{29}$$

Then, substituting (27)–(29) into (24) and (25), we obtain the following forms for the boundary conditions at $O(\epsilon^2)$:

$$\frac{\partial f_2}{\partial \tilde{t}} - \frac{\partial \phi_2}{\partial r} = \sum A_{mk}\,\mathrm{e}^{\mathrm{i}m\tilde{t}} P_k(\eta) + \text{c.c.}, \tag{30}$$

$$\omega_n^2 \frac{\partial \phi_2}{\partial \tilde{t}} + (\nabla_s^2 + 2) f_2 - (4\omega_n^2 + 2)\langle f_2 \rangle = \sum B_{mk}\,\mathrm{e}^{\mathrm{i}m\tilde{t}} P_k(\eta) + \text{c.c.}, \tag{31}$$

where $m = 1, 2, 3, 4$, and $k = 0, 2, 4, \ldots, 2n$ and also $k = n$ (the expansion of $P_n^2(\eta)$ gives rise to terms $P_0(\eta)$, $P_2(\eta)$, $\ldots$, $P_{2n}(\eta)$). Among the values of A_{mk} and B_{mk}, only the following four are needed in the later calculations:

$$A_{20} = \frac{-1}{2(2n+1)\omega_n}\left(\frac{\mathrm{d}\alpha_{1,0}}{\mathrm{d}\tau} + 2n\,\alpha_{1,0} - \mathrm{i}\omega_n\,\alpha_{1,n}^2\right), \tag{32a}$$

$$B_{20} = \mathrm{i}\omega_n \frac{\mathrm{d}\alpha_{1,0}}{\mathrm{d}\tau} + (4\mathrm{i}\omega_n\,\tilde{S} - 4\omega_n\,\sigma_n + 2\beta_0\,\omega_n)\,\alpha_{1,0} + \frac{(n-1)(n+2)(12n+7)}{8(2n+1)}\alpha_{1,n}^2 + \tfrac{1}{2}\tilde{A}_0, \tag{32b}$$

$$A_{1n} = -\frac{1}{2\omega_n}\frac{\mathrm{d}\alpha_{1,n}}{\mathrm{d}\tau} + \frac{\mathrm{i}(n-2)}{4}\alpha_{1,0}\,\alpha_{1,n}^*, \tag{32c}$$

$$\begin{aligned} B_{1n} = {} & \frac{\mathrm{i}\omega_n}{2(n+1)}\frac{\mathrm{d}\alpha_{1,n}}{\mathrm{d}\tau} + \frac{\tilde{A}_n}{2} + \left[\frac{\mathrm{i}(2n+1)(n+2)\,\omega_n}{n+1}\tilde{S} - \frac{\omega_n\,\sigma_n}{n+1}\right]\alpha_{1,n} \\ & + \frac{(n-1)(n+2)(3n+1)}{4}\alpha_{1,0}\,\alpha_{1,n}^*, \end{aligned} \tag{32d}$$

where a superscript * denotes complex conjugate of the variable.

To solve for ϕ_2 and f_2, we can use the method of superposition. However, as we proceed, we encounter secular terms which cause the solution at $O(\epsilon^2)$ to be unbounded unless certain conditions are satisfied. Imposing these conditions for boundedness of the solution at $O(\epsilon^2)$, we obtain dynamical equations for the $O(\epsilon)$ amplitude functions $\alpha_{1,0}$ and $\alpha_{1,n}$ given in the following section.

3. Solvability conditions and amplitude equations

Using the method of superposition, we assume

$$f_2 = \sum a_{mk} \mathrm{e}^{\mathrm{i}m\tilde{t}} P_k(\eta) + \text{c.c.}, \quad \phi_2 = \sum b_{mk} r^{-(k+1)} \mathrm{e}^{\mathrm{i}m\tilde{t}} P_k(\eta) + \text{c.c.} \qquad (33a,b)$$

and substitute these expressions into the boundary conditions (30), and (31) to obtain algebraic equations for a_{mk} and b_{mk}. For $k = 0$, we find

$$\begin{pmatrix} \mathrm{i}m & 1 \\ -4\omega_n^2 & \mathrm{i}m\omega_n^2 \end{pmatrix} \begin{pmatrix} a_{m0} \\ b_{m0} \end{pmatrix} = \begin{pmatrix} A_{m0} \\ B_{m0} \end{pmatrix}, \qquad (34)$$

and for $k \neq 0$,

$$\begin{pmatrix} \mathrm{i}m & k+1 \\ -(k-1)(k+2) & \mathrm{i}m\omega_n^2 \end{pmatrix} \begin{pmatrix} a_{mk} \\ b_{mk} \end{pmatrix} = \begin{pmatrix} A_{mk} \\ B_{mk} \end{pmatrix}. \qquad (35)$$

It is easy to see that the matrix in (34) is singular when $m = 2$ and the matrix in (35) is singular if $m = 1$ and $k = n$. In these two special cases, if a_{20}, b_{20}, a_{1n}, and b_{1n} are to remain bounded, the vectors on the right-hand sides of (34) and (35) have to be perpendicular to the left-eigenvectors corresponding to zero eigenvalue of the matrices in (34) and (35) respectively. The two left-eigenvectors corresponding to zero eigenvalue of the matrices in (34) and (35) are

$$(2\mathrm{i}\omega_n^2, -1) \quad \text{and} \quad (\mathrm{i}\omega_n^2, -3).$$

Hence, we obtain

$$2\mathrm{i}\omega_n^2 A_{20} - B_{20} = 0 \quad \mathrm{i}\omega_n^2 A_{1n} - 3B_{1n} = 0. \qquad (36a,b)$$

Substituting the coefficients (32) into these equations, we obtain the following equations for the slowly varying amplitude functions of the $O(\epsilon)$ solution, (27) and (28),

$$\frac{\mathrm{d}\alpha_{1,0}}{\mathrm{d}\tau} = -2\tilde{S}\alpha_{1,0} + (\beta_0 - 2\sigma_n)\mathrm{i}\alpha_{1,0} + \mathrm{i}\frac{1}{4\omega_n}\tilde{A}_0 + \mathrm{i}H_5\alpha_{1,n}^2, \qquad (37a)$$

$$\frac{\mathrm{d}\alpha_{1,n}}{\mathrm{d}\tau} = -N\tilde{S}\alpha_{1,n} - \mathrm{i}\sigma_n\alpha_{1,n} + \mathrm{i}\frac{n+1}{2\omega_n}\tilde{A}_n + \mathrm{i}H_6\alpha_{1,0}\alpha_{1,n}^*, \qquad (37b)$$

and

$$N = (n+2)(2n+1), \qquad (38)$$

and

$$H_5 = \frac{(4n-1)\,\omega_n}{16(n+1)(2n+1)}, \quad H_6 = \frac{(4n-1)\,\omega_n}{4}, \qquad (39a,b)$$

as defined in Yang *et al.* (1993).

It may be noted that the procedure described above for derivation of the amplitude equations (37) is discussed in detail in Nayfeh & Mook (1979), and the interested reader may find this reference useful in understanding the present work. In any case, the amplitude equations, in the undamped and unforced case, that is when $\tilde{S}$, $\tilde{A}_0$, and $\tilde{A}_n$ are identically zero, agree with the amplitude equations of Feng & Leal (1993) for the quadratic resonance case, which were shown earlier (by Yang *et al.* 1993) to agree with those of Ffowcs Williams & Guo (1991) and Longuet-Higgins (1991). When

$\tilde{A}_n = 0$, the form of (37) also agrees with the governing equations of Mei & Zhou (1991).

In (37), the terms associated with $\tilde{S}$ are due to the weak viscous effect. They are identical to those of Lamb (1932). From the expression for N, we note that the dissipation associated with higher modes is much stronger than that of the lower modes. The terms involving $\tilde{A}_0$ and $\tilde{A}_n$ are due to isotropic and anisotropic pressure forcing respectively. As explained in Feng & Leal (1993), the quadratic coupling terms associated with H_5 and H_6 are caused by the nonlinearity of the boundary conditions.

Finally, we should note that the nonlinear resonance terms in (37) are quadratic by assumption. Cubic terms which would reflect the nonlinearity of individual mode oscillation, such as the dependence of free oscillation frequencies upon the amplitudes, are of higher order and thus not included in our amplitude equations. Consequently, when the shape mode has a zero amplitude, the amplitude equation for $\alpha_{1,0}$ is linear, which is equivalent to the *linearized* Rayleigh–Plesset equation after the averaging procedure is applied.

In order to see the effect of detuning from exact resonance, i.e. of non-zero values for σ_n and β_0, we set $\tilde{S}$, $\tilde{A}_0$, and $\tilde{A}_n$ to zero and neglect the quadratic nonlinear terms. Then solving (37), we obtain

$$\alpha_{1,0}(\tau) = C_0\,\mathrm{e}^{(\beta_0-2\sigma_n)\tau}, \quad \alpha_{1,n}(\tau) = C_n\,\mathrm{e}^{-\sigma_n\tau},$$

where C_0 and C_n are constants determined by the initial conditions. Substituting these into (27) and recalling that $\tilde{t} = \Omega t$, $\tau = \epsilon t$, we have

$$f_1 = \tfrac{1}{2}\{\alpha_{1,0}(\tau)\,\mathrm{e}^{2\mathrm{i}\Omega t+\epsilon(\beta_0-2\sigma_n)t} + \alpha_{1,n}(\tau)\,\mathrm{e}^{\mathrm{i}\Omega t-\epsilon\sigma_n t}\,P_n(\eta)\} + \mathrm{c.c}$$

From (15) and (16), we have

$$2\Omega + \epsilon(\beta_0 - 2\sigma_n) = \omega_0, \quad \Omega - \epsilon\sigma_n = \omega_n.$$

We see that the breathing mode is oscillating at ω_0 and the shape mode is oscillating at ω_n, as they should. Hence terms associated with σ_n and β_0 restore the frequencies of small-amplitude free oscillation of the two modes to their respective natural frequencies. The parameters σ_n and β_0 are known as the external and internal frequency detuning parameters, respectively. When $\sigma_n = 0$, the external periodic forcing is in exact resonance with the shape mode. When $\sigma_n = \tfrac{1}{2}\beta_0$, the external periodic forcing is in exact resonance with the volume mode.

Note that none of the constants in (37) depends on whether the bubble is a gas bubble or a vapour bubble. This implies that our amplitude equations are equally valid for studying the dynamics of ideal gas bubbles and isothermal vapour bubbles. This seems inconsistent with the known difference between an ideal spherical gas bubble and an isothermal spherical vapour bubble as described by the Rayleigh–Plesset model. An ideal spherical gas bubble in an inviscid fluid will undergo periodic oscillation for any initial perturbation of the bubble radius, see Smereka *et al.* (1987). However, the same is not true for a vapour bubble. Szeri & Leal (1991) have shown that for a vapour bubble there exists a critical initial perturbation of the bubble radius, above which the bubble radius will grow to unbounded values. Periodic oscillation of vapour bubbles is only possible for perturbations below this critical value. This is because expansion of the radius of a vapour bubble leads to a diminished restoring surface tension force but with an unabated vapour pressure inside the bubble. For the gas bubble, on the other hand, the gas pressure inside the bubble decreases as the volume increases, and this provides a restoring force of increasing magnitude to resist bubble growth. Why is the difference between the two types of bubbles not reflected in our amplitude equation (37)? The answer, as stated earlier, is that we neglect terms beyond quadratic in the amplitude equations, which means that we retain only the linear approximation of the Rayleigh–Plesset equation. At that level of approximation, the difference between the gas bubble and the vapour bubble is absent.

We observe that for fixed n, the dynamical system (37) depends on four parameters. These parameters are $\tilde{S}$, σ_n, β_0, and Δ_0 (or Δ_n) which correspond to the dimensionless magnitude of the viscosity, the external frequency detuning, the internal frequency detuning and the magnitude of the periodic forcing respectively. In order to simplify the equations, we let

$$\alpha_{1,0} = N\tilde{S}\frac{1}{H_6}\alpha_0, \quad \alpha_{1,n} = N\tilde{S}\frac{1}{(H_5 H_6)^{\frac{1}{2}}}\alpha_n \tag{40a,b}$$

$$\Delta_0 = \frac{H_6}{4(N\tilde{S})^2\omega_n}\tilde{A}_0, \quad \Delta_n = \frac{(n+1)(H_5 H_6)^{\frac{1}{2}}}{2\omega_n(N\tilde{S})^2}\tilde{A}_n, \tag{40c,d}$$

$$\beta = \beta_0/(N\tilde{S}), \quad \sigma = \sigma_n/(N\tilde{S}) \tag{40e,f}$$

to obtain

$$\dot{\alpha}_0 = -(2/N)\alpha_0 + \mathrm{i}(\beta - 2\sigma)\alpha_0 + \mathrm{i}\Delta_0 + \mathrm{i}\alpha_n^2, \tag{41a}$$

$$\dot{\alpha}_n = -\alpha_n - \mathrm{i}\sigma\alpha_n + \mathrm{i}\Delta_n + \mathrm{i}\alpha_0\alpha_n^*, \tag{41b}$$

where the dot stands for differentiation with respect to $N\tilde{S}\tau$. The parameters Δ_0, Δ_n, σ, β are proportional to $\tilde{A}_0$, $\tilde{A}_n$, σ_n, and β_0. They correspond to the magnitude of the forcing amplitudes and detuning parameters *relative* to the dissipation. The limit $\beta = 0$ corresponds to exact internal resonance, while $\sigma = 0$ and $\sigma = \frac{1}{2}\beta$ correspond to the two exact external resonance cases.

We note that (41) possess 'parameter symmetry': if we change $(\beta, \sigma, \alpha_0, \alpha_n)$ into $(-\beta, -\sigma, -\alpha_0^*, -\alpha_n^*)$, the new dynamical system is identical to (41). Therefore, we only need to study the dynamics for positive values of β and obtain the result for negative β by a simple reflection. In the following analysis, we will asume $\beta \geqslant 0$.

To carry out an analysis of the system (41), it is often convenient to introduce the transformation

$$\alpha_0 = r_0 \mathrm{e}^{\mathrm{i}\theta_0}, \quad \alpha_n = r_n \mathrm{e}^{\mathrm{i}\theta_n} \tag{42}$$

in order to write this dynamical system in double polar coordinates:

$$\dot{r}_0 = -\frac{2}{N}r_0 - r_n^2\sin(2\theta_n - \theta_0) + \Delta_0\sin\theta_0, \tag{43a}$$

$$\dot{\theta}_0 = \beta - 2\sigma + \frac{r_n^2}{r_0}\cos(2\theta_n - \theta_0) + \frac{\Delta_0}{r_0}\cos\theta_0, \tag{43b}$$

$$\dot{r}_n = -r_n + r_0 r_n\sin(2\theta_n - \theta_0) + \Delta_n\sin\theta_n, \tag{43c}$$

$$\dot{\theta}_n = -\sigma + r_0\cos(2\theta_n - \theta_0) + \frac{\Delta_n}{r_n}\cos\theta_n, \tag{43d}$$

However, one disadvantage of the polar form (43) is that it is singular at $r_0 = 0$ or $r_n = 0$, which is an artifact of the use of polar coordinates, i.e. when $r_0 = 0$ or $r_n = 0$, θ_0 and θ_n are undefined. To compensate for this disadvantage, we can also write (41) in terms of rectangular coordinates by letting $\alpha_0 = x_0 + \mathrm{i}y_0$, $\alpha_n = x_n + \mathrm{i}y_n$ to obtain

$$\dot{x}_0 = -\frac{2}{N}x_0 - (\beta - 2\sigma)y_0 - 2x_n y_n, \quad \dot{y}_0 = (\beta - 2\sigma)x_0 - \frac{2}{N}y_0 + x_n^2 - y_n^2 + \Delta_0, \tag{44a,b}$$

$$\dot{x}_n = -x_n + \sigma y_n - (y_0 x_n - x_0 y_n), \quad \dot{y}_n = -\sigma x_n - y_n + x_0 x_n + y_0 y_n + \Delta_n. \tag{44c,d}$$

Equations (44) are uniformly valid and are made more general in the Appendix. They are, in fact, used for much of the subsequent analysis and for all numerical computation. Nevertheless, if the singularity at $r_0 = 0$ or $r_n = 0$ can be avoided, system (43) is algebraically more convenient to use. Furthermore, since r_0 and r_n are directly proportional to the physical amplitudes of the volume and shape modes, we will generally use them to present our results even when the analysis or computation has been done using the rectangular coordinate form, (44).

Since the rest of this paper will be based on a study of the amplitude equations (41), in either the form (43) or (44), it is convenient to summarize the relationship between the present variables and the physical variables. By physical variables we mean the dimensionless variables scaled by l_c, t_c, and p_c. Starting from (40), we see that once α_0 and α_n are determined, accurate up to $O(\epsilon)$, the physical amplitudes of the two modes in complex form are

$$\epsilon\alpha_{1,0} = \frac{4(n+2)(2n+1)}{(4n-1)\,\omega_n} S\alpha_0, \quad \epsilon\alpha_{1,n} = \frac{(4n-1)(n+2)\,\omega_n}{8}\left(\frac{2n+1}{n+1}\right)^{\frac{1}{2}} S\alpha_n, \tag{45}$$

respectively. In deriving the above, formulae (12), (18), (27), (38) and (39) have been used. The parameters in (41) (or (43) and (44)) are related to physical parameters according to the following formulae:

$$\Delta_0 = \frac{4n-1}{16[(n+2)(2n+1)]^2}\frac{A_0}{S^2}, \quad \Delta_n = \frac{4n-1}{16[(n+2)(2n+1)]^2}\left(\frac{n+1}{2n+1}\right)^{\frac{1}{2}}\frac{A_n}{S^2}, \tag{46a,b}$$

$$\beta = \frac{\omega_0 - 2\omega_n}{(n+2)(2n+1)\,S}, \quad \sigma = \frac{\Omega - \omega_n}{(n+2)(2n+1)\,S}. \tag{46c,d}$$

All quantities on the right-hand side of (46) are physical quantities. The time-like variable implicit in (41), (43) and (44) is $(n+2)(2n+1)\,St$, where t is the dimensionless time. Note that the small parameter ϵ does not occur explicitly in (46).

Finally, it is perhaps useful to emphasize that the *fixed points* of the slow-time-variable dynamical system, (41), in either of the forms (44) or (43), correspond to *periodic motions* of the bubble on the short timescale, $\tilde{t}$. This can be seen clearly by recalling the relationship (27). In the form (43), the meaning of 'fixed point' is that $\dot{r}_0, \dot{r}_n, \dot{\theta}_0$ and $\dot{\theta}_n$ are *all* zero, and the same is true of $\dot{x}_0, \dot{x}_n, \dot{y}_0$ and $\dot{y}_n$ in (44). This may be contrasted with the polar representation of a typical two-variable dynamical system (cf. Guckenheimer & Holmes 1983, §1.5) in which periodic orbits correspond simply to fixed points of the amplitude function r only (a point of confusion with one of our referees).

One of our objectives in this paper is to study the stability of spherical bubble oscillations under non-spherical perturbations. The amplitude equations in (41), in the special case of $\Delta_n = 0$, are suitable for this purpose. However, in deriving these equations, we have required that the natural frequencies of the volume mode and the shape mode satisfy the resonance condition (15). Intuitively, we expect that the stability of the volume mode should only depend on the amplitude of the volume mode and be independent of this resonance condition. Hence, before we move on to study the amplitude equations (41), we derive another set of amplitude equations that are valid when the internal resonance condition (15) is not satisfied.

4. Generalization of the amplitude equations to include the internally non-resonant case

Consider an isotropically forced bubble oscillation. Assume that the forcing frequency (2Ω) is approximately twice that of the shape mode, so that (16) holds. At the same time, we assume that the natural frequency of the volume mode is not close to 2Ω, i.e. (15) is violated. Then in order to generate an $O(\epsilon)$ volume response, the magnitude of forcing has to be of $O(\epsilon)$ instead of $O(\epsilon^2)$. That is

$$A_0 = \epsilon \tilde{A}_0$$

For this case, the governing equation at $O(\epsilon)$ is

$$\nabla^2 \phi_1 = 0 \tag{47}$$

but the boundary conditions at $r = 1$ become

$$\frac{\partial f_1}{\partial \tilde{t}} - \frac{\partial \phi_1}{\partial r} = 0, \tag{48a}$$

$$\omega_n^2 \frac{\partial \phi_1}{\partial \tilde{t}} + (\nabla_s^2 + 2) f_1 - (\omega_0^2 + 2)\langle f_1 \rangle = \tilde{A}_0 \cos 2\tilde{t}. \tag{48b}$$

Substituting (27) and (28) into the above, we find that (47) and (48) are satisfied by

$$\alpha_{1,0} = \frac{\tilde{A}_0}{4\omega_n^2 - \omega_0^2} \tag{49}$$

with *arbitrary* $\alpha_{1,n}$. The denominator of (49) is of $O(1)$ since (15) is violated by assumption. The solution (49) corresponds to a radial oscillation at $O(\epsilon)$ on the same timescale as the pressure forcing.

In this case at $O(\epsilon^2)$, we obtain

$$\nabla^2 \phi_2 = 0,$$

and the boundary conditions at $r = 1$

$$\frac{\partial f_2}{\partial \tilde{t}} - \frac{\partial \phi_2}{\partial r} = \sum A_{mk} \mathrm{e}^{\mathrm{i}m\tilde{t}} P_k(\eta) + \text{c.c.},$$

$$\omega_n^2 \frac{\partial \phi_2}{\partial \tilde{t}} + (\nabla_s^2 + 2) f_2 - (\omega_0^2 + 2)\langle f_2 \rangle = \sum B_{mk} \mathrm{e}^{\mathrm{i}m\tilde{t}} P_k(\eta) + \text{c.c.}$$

Since $4\omega_n^2 - \omega_0^2 = O(1)$, instead of two solvability conditions we now obtain only one solvability condition, which is

$$\frac{\mathrm{d}\alpha_{1,n}}{\mathrm{d}\tau} = -N\tilde{S}\alpha_{1,n} - \mathrm{i}\sigma_n \alpha_{1,n} + \mathrm{i}H_6 \alpha_{1,0} \alpha_{1,n}^*. \tag{50}$$

We see that (50) is identical to (37*b*). However, the interpretation of (49) and (50) is different from the interpretation of (37). In (37), the two modes $\alpha_{1,0}$ and $\alpha_{1,n}$ are competing modes, hence the dynamics are more interesting, with the possibility of interchange of energy back and forth, between shape and volume oscillation. In (49) and (50), on the other hand, the two modes are like a master and a slave. The amplitude of the volume mode, $\alpha_{1,0}$, is completely determined by the forcing, equation (49), and the dynamics of $\alpha_{1,n}$ is completely determined by its master $\alpha_{1,0}$ through (50).

Later, we shall use (37) to discuss the stability of the purely radical oscillation to non-spherical perturbations. The above discussion shows that any result based on (37) can be equally applied to the case when the isotropic forcing frequency is not near the natural frequency of the volume mode, an assumption used in deriving (37).

5. Dynamics of an isotropically forced bubble, $\Delta_n = 0$

In the remaining sections, we study bubble dynamics based on the analysis and simulation of the amplitude equations (43) or (44), whichever is more appropriate. The results of our analysis will be presented in the form of bifurcation sets and bifurcation diagrams. The bifurcation sets delineate the regions of parameter space, including forcing frequency and forcing amplitude, within which the qualitative behaviour of the system, e.g. the number of fixed points and their stability, remains the same. The bifurcation diagrams show the bubble response, e.g. the amplitudes of the volume and shape modes, plotted against one control parameter (the driving frequency or amplitude). The simulations were done using a fourth order Runge–Kutta integration routine from IMSL.

The isotropically forced case, $\Delta_n = 0$, has been studied by Mei & Zhou (1991). In the absence of internal detuning $\beta = 0$, Mei & Zhou did not find a chaotic response. Instead chaos was found only for non-zero values of β. Their work suggests that there exists a critical β_c, below which no chaos can occur. Our goal in the present section is to calculate β_c, and to determine bifurcation sets and obtain bifurcation diagrams that completely describe the dynamics. As indicated in the introduction, this information should be indispensable for guiding experimental studies, and explaining experimental results.

The bifurcation analysis of the system (41) starts with the fixed points and an analysis of their stability. Analysis of this kind, for the special case of $\beta = 0$, has been done by Sethna (1965) and Miles (1984*b*) in the context of nonlinear oscillators. We present a more general treatment here. The equations in the double polar form, (43), are best suited for fixed-point analysis. We observe that there are two types of fixed points, those with $r_n = 0$ and those with $r_n \neq 0$.

Fixed-point solutions with $r_n = 0$ physically correspond to purely radial oscillations of spherical bubbles. Solving (43*a*) and (43*b*) for r_0 and θ_0 at fixed points ($\dot{r}_0 = 0$, $\dot{\theta}_0 = 0$) with $r_n = 0$, we find

$$r_0^2 = \frac{\Delta_0^2}{4/N^2 + (\beta - 2\sigma)^2}, \quad \tan\theta_0 = -\frac{2}{N(\beta - 2\sigma)}. \tag{51}$$

This solution corresponds to a purely radial oscillation at the frequency of the forcing (2Ω) in dimensionless physical time. The stability of this solution to both spherical and non-spherical perturbations can be determined by calculating the eigenvalues of the Jacobian matrix of the system in the form (44), with (51) substituted. Among the four eigenvalues of the Jacobian matrix, two are given by the eigenvalues of the matrix

$$\begin{pmatrix} -2/N & -(\beta - 2\sigma) \\ \beta - 2\sigma & -2/N \end{pmatrix}$$

whose trace is negative and determinant is positive. Hence these two eigenvalues lie on the left half of the complex plane. The other two eigenvalues are given by the eigenvalues of the matrix

$$\begin{pmatrix} -1 - y_0 & \sigma + x_0 \\ -\sigma + x_0 & -1 + y_0 \end{pmatrix}.$$

It follows that the solution (51) is stable if and only if

$$1+\sigma^2-(x_0^2+y_0^2) > 0,$$

or, if expressed in terms of the amplitude r_0,

$$r_0^2 < 1+\sigma^2. \tag{52}$$

Owing to the change of variables introduced in (40), this criterion obviously has a very simple form. By making substitutions summarized in (45) and (46), (52) can easily be expressed in terms of physical parameters, namely the amplitude of the volume oscillation, the external frequency detuning, and the viscosity factor S. The result will be given and discussed in §7.

If we substitute (51) into (52), we have conditions for the stability of the solution (51) in parameter space:

$$\Delta_0 < \{(1+\sigma^2)[4/N^2+(\beta-2\sigma)^2]\}^{\frac{1}{2}}. \tag{53}$$

Again this inequality can be expressed in terms of physical parameters by using (46). Note that condition (52) does not involve the internal frequency detuning parater β, hence it is also valid for the internally non-resonant case discussed in §4. Condition (53), on the other hand, is expressed in terms of the forcing amplitude, and does involve the internal frequency detuning parameter β. Hence it is valid only for the internally resonant case. Violation of either of the inequalities (52) or (53) indicates that the pure radial oscillation is unstable to non-spherical perturbations. This will also become clearer later as we discuss bifurcation diagrams.

Fixed-point solutions with $r_n \neq 0$ correspond to non-spherical bubble oscillations. Since $r_n \neq 0$, solving (43*c*) and (43*d*) for r_0 and $2\theta_n-\theta_0$, we obtain

$$r_0^2 = 1+\sigma^2, \quad \tan(2\theta_n-\theta_0) = 1/\sigma, \tag{54}$$

which can be substituted into (43*a*) and (43*b*). After eliminating θ_0 we obtain

$$r_n^4+2[2/N+\sigma(\beta-2\sigma)]\,r_n^2+(1+\sigma^2)[4/N^2+(\beta-2\sigma)^2]-\Delta_0^2 = 0. \tag{55}$$

Equation (55) is a quadratic equation for r_n^2, which has real solutions only when

$$\Delta_0 > |\beta-2\sigma-2\sigma/N|. \tag{56}$$

Physically, this means that non-spherical bubble oscillations can only be driven by an isotropic pressure fluctuation with an amplitude above some critical value. In general there are two branches of solutions when (56) is satisfied;

$$r_n^2 = -[2/N+\sigma(\beta-2\sigma)] \pm [\Delta_0^2-(\beta-2\sigma-2\sigma/N)^2]^{\frac{1}{2}}. \tag{57}$$

We denote the solutions corresponding to + and − signs as branch 1 and branch 2 respectively.

The stability of these branches is gain determined by the eigenvalues of the Jacobian matrix of the system (44), in this case evaluated with (57). The eigenvalues of the Jacobian matrix are given by the roots of the polynomial

$$J_4\lambda^4+J_3\lambda^3+J_2\lambda^2+J_1\lambda+J_0 = 0, \tag{58}$$

where

$$J_4 = 1, \quad J_3 = 2+4/N, \quad J_2 = 4r_n^2+4(1+2N)/N^2+(\beta-2\sigma)^2,$$
$$J_1 = 4r_n^2(1+2/N)+8/N^2+2(\beta-2\sigma)^2, \quad J_0 = \pm 4r_n^2[\Delta_0^2-(\beta-2\sigma-2\sigma/N)^2]^{\frac{1}{2}}. \tag{59}$$

Following the Routh–Hurwicz criteria, a fixed point is stable if

$$\text{(i) } J_0 > 0, \quad \text{(ii) } J_1 > 0, \quad \text{(iii) } J_3J_4 > 0, \quad \text{(iv) } J_1(J_2J_3-J_1J_4)-J_0J_3^2 > 0.$$

It is obvious that branch 2 violates condition (i), and is therefore never stable. Branch 1 satisfies the first three conditions, while condition (iv) becomes

$$P+Qr_n^2 > 0,$$

where $$P = 8/N^5[4+N^2(\beta-2\sigma)^2][4(N+1)^2+N^2(\beta-2\sigma)^2] \tag{60}$$

and $$Q = 8(2+N)^2/N^4\{4(1+N)+N^2[8(\sigma-3\beta/8)^2-\beta^2/8]\}. \tag{61}$$

Since the coefficient P is always positive, a conservative condition for the stability of the constant-amplitude, non-spherical bubble oscillations corresponding to branch 1 is that $Q \geqslant 0$, which is the case for

$$\beta^2 < \beta_c^2,$$

where $$\beta_c \equiv [32(N+1)]^{\frac{1}{2}}/N. \tag{62}$$

Thus, provided there is a sufficiently close match between the natural frequencies, ω_0 and ω_n, the bubble can sustain stable, non-spherical oscillations when subjected to an isotropic pressure forcing with amplitude satisfying the condition (56).

When the equality holds in condition (iv), Hopf bifurcation occurs, which physically corresponds to a transition from constant-amplitude (non-spherical) oscillations to an amplitude-modulated oscillation of the bubble. This can be easily shown by noting that at a Hopf bifurcation point, there is a pair of pure imaginary eigenvalues, hence the characteristic equation (58) can be put in the form

$$(\lambda^2+\omega^2)(\lambda^2+a\lambda+b) = 0,$$

which is possible only when equality holds for condition (iv), namely

$$P+Qr_n^2 = 0. \tag{63}$$

We observe that P is always positive, and Q is positive for

$$\beta^2 < \beta_c^2.$$

Therefore, for $\beta < \beta_c$, no Hopf bifurcation occurs and branch 1 remains stable. The exact location of the Hopf bifurcation point depends on the parameter Δ_0. Substituting (57) into (63), we get

$$(\Delta_0)_{Hopf} = \left\{\left[\beta-2\sigma-\frac{2}{N}\right]^2+\left[\frac{2}{N}+\sigma(\beta-2\sigma)-\frac{P}{Q}\right]^2\right\}^{\frac{1}{2}}. \tag{64}$$

For a fixed value of Δ_0, by solving (64) we can obtain values of σ, denoted σ_{H1} and σ_{H2} ($\sigma_{H1} < \sigma_{H2}$) which may depend on β, for which Hopf bifurcation occurs. Obviously, real solutions of (64) for σ exist only for $Q < 0$, which requires $\beta > \beta_c$. Furthermore, it can be shown that

$$\frac{3\beta}{8}-\left(\frac{\beta^2}{64}-\frac{N+1}{2N^2}\right)^{\frac{1}{2}} < \sigma_{H1} < \sigma_{H2} < \frac{3\beta}{8}+\left(\frac{\beta^2}{64}-\frac{N+1}{2N^2}\right)^{\frac{1}{2}}.$$

Since $N > 0$, we observe that the Hopf bifurcation points lie within the interval

$$\tfrac{1}{4}\beta < \sigma_{H1} < \sigma_{H2} < \tfrac{1}{2}\beta.$$

The boundaries defined by (53) and (56), combined with (64), divide the parameter space into finite sets. For fixed values of N and β, the parameter space is two-dimensional (σ, Δ_0). For $N = 20$ ($n = 2$) and $\beta = 0$, these boundaries (53) and (56) are plotted in figure 2. $(\Delta_0)_{Hopf}$ is not plotted since no Hopf bifurcation exists for $\beta < \beta_c$, $\beta_c = 1.29$. It appears that the two straight lines, corresponding to (56), intersect the

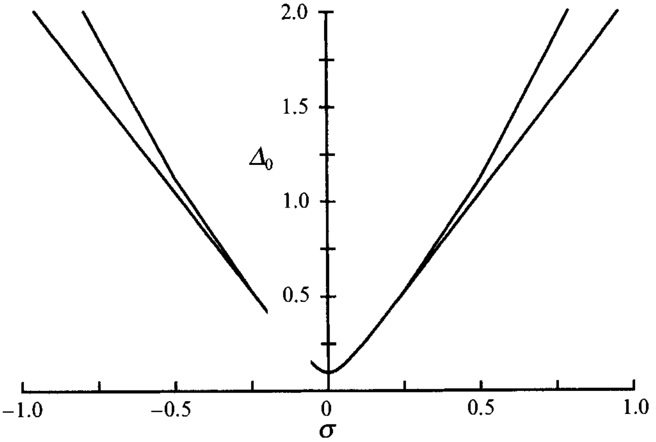

FIGURE 2. The curves defined by (53) and (56) in the parameter space (σ, Δ_0), $\beta = 0$.

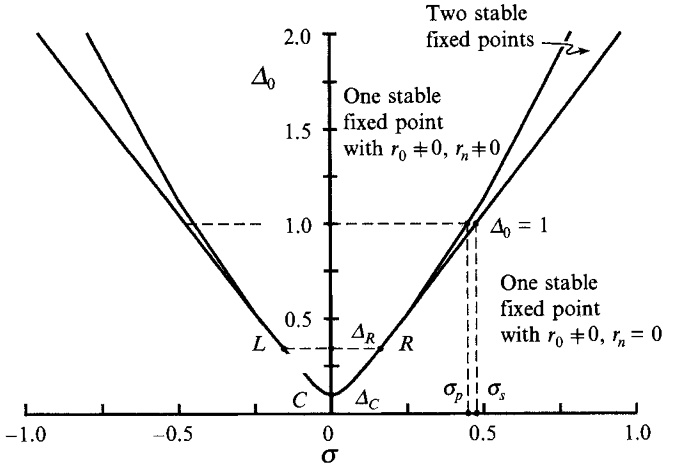

FIGURE 3. Bifurcation sets in the (σ, Δ_0) space for $\beta = 0$. No Hopf bifurcation occurs in this case. Note that some line segments which do not correspond to any bifurcation have been removed.

curve, corresponding to (53), tangentially. This can be shown by first calculating the intersection points (for arbitrary β and N):

$$\sigma = \frac{N\beta \pm (N^2\beta^2 - 16N)^{\frac{1}{2}}}{4N}, \quad \Delta_0 = \left| \frac{\beta(N-1)}{2N} \mp \frac{1+N}{2N^2}(N^2\beta^2 + 16N)^{\frac{1}{2}} \right|. \tag{65}$$

We then show that the derivatives with respect to σ of both boundaries are the same at the intersection point. Furthermore, numerical work indicates that line segments below the intersection points do not correspond to any bifurcation. They are thus omitted.

We present in the following the detailed bifurcation analysis for three representative cases, $\beta = 0$, 2 and 1.

5.1. $\beta = 0$

Figure 3 shows the bifurcation set for $N = 20$ $(n = 2)$ and $\beta = 0$. Two straight lines, given by (56), and a 'parabolically' shaped curve, given by (53), divide the parameter space (σ, Δ_0) into four open sets. In the set below the lines and the curve, there is one stable fixed point with the property $r_n = 0$. This corresponds to radial oscillations of

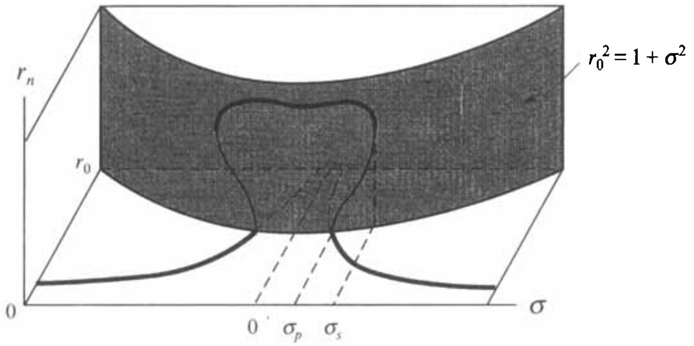

FIGURE 4. Schematic bifurcation diagram for $\beta = 0$ and $\Delta_0 > (\Delta_0)_L$. Thick lines, stable; thin lines, unstable.

the bubble with the shape of the bubble remaining spherical. In the region inside the parabolically shaped curve, there is one stable fixed point with the property $r_n \neq 0$. This corresponds to bubble oscillations where shape oscillation has set in due to the instability of the spherical bubble oscillations. The fact that this solution is stable means that any small perturbation, whether spherical or non-spherical, will not change the dynamics of the bubble except on a very short time period. Inside the two wedges, both of the above two fixed points exist. There are two possible types of stable bubble oscillations. In this case, after a brief transient, the bubble will settle to one or the other of these constant-amplitude oscillations, depending on the initial conditions.

To understand how bifurcation takes place as the system parameters are changed, we first take a horizontal cut of figure 3 above the two intersection points L and R and draw a schematic bifurcation diagram by plotting r_0 and r_n versus σ. This bifurcation diagram, figure 4, corresponds to response curves for fixed forcing amplitude, $\Delta_0 = 1$, as the forcing frequency is slowly detuned. The values σ_p and σ_s correspond to σ-values at the intersection points of the horizontal line $\Delta_0 =$ const with the two curves in figure 3. They can be determined by solving (53) and (56) for σ with $\Delta_0 \equiv 1$. Since the bifurcation diagram is symmetric with respect to the plane $\sigma = 0$ in the three-dimensional space (σ, r_0, r_n), we describe the bifurcation sequences for $\sigma > 0$. For large σ, thus high forcing frequency according to (46), the response curve lies in the plane $r_n = 0$, and the bubble oscillation therefore remains spherical. At $\sigma = \sigma_p$, a subcritical pitchfork bifurcation occurs, where the spherical shape of the bubble loses stability. The stable fixed point for the amplitude functions jumps onto the mushroom-shaped curve on the hyperbolic surface $r_0^2 = 1 + \sigma^2$. Associated with this transition, a large-amplitude shape oscillation sets in. If we increase the forcing frequency from that point on, the shape oscillation remains for σ above σ_p. However, eventually it loses stability at a saddle node bifurcation at σ_s. Hence on the interval (σ_p, σ_s), a hysteresis phenomenon occurs.

The pitchfork bifurcation at σ_p seems unconventional in the sense that one expects the number of fixed points to change from one to three. The reason why this does not appear to be the case here, is because of the choice of coordinate axis of our bifurcation diagram. It is important to realize that since $\Delta_n = 0$, if $(r_0(t), \theta_0(t), r_n(t), \theta_n(t))$ is a solution (43), so is $(r_0(t), \theta_0(t), r_n(t), \theta_n(t) + \pi)$. Therefore, for the branch bifurcating from the plane $r_n = 0$ in figure 4, there is a mirror image. Here the mirror is the horizontal plane $r_n = 0$.

The bifurcation diagram for a fixed value of Δ_0 which lies between Δ_C and Δ_L (or Δ_R) is similar to figure 4. Since the two straight lines in figure 3, which correspond to the

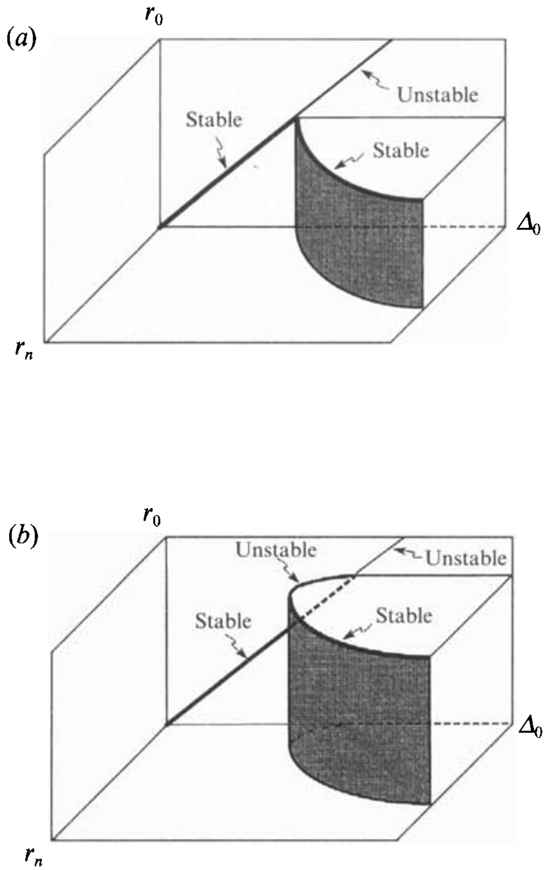

FIGURE 5. Schematic bifurcation diagram for $\beta = 0$ and for fixed value of σ. (*a*) $(\sigma)_L < \sigma < (\sigma)_R$. (*b*) $\sigma < (\sigma)_L$, or $\sigma > (\sigma)_R$. Thick lines, stable; thin lines, unstable.

saddle node bifurcations terminate at points marked L and R, a horizontal line of $\Delta_0 = \text{const} < \Delta_L$ will not intersect any saddle-node bifurcation. Hence the curve on the hyperbolic surface in figure 4 will be arch shaped instead of mushroom shaped. No jump phenomenon occurs. The transition to and from the shape mode is continuous and the pitchfork bifurcation at σ_p is supercritical.

For $\Delta_0 < \Delta_C$ no bifurcation occurs. The response curve lies on the plane $r_n = 0$ with a small peak at $\sigma = 0$. Thus Δ_C is a threshold, below which no shape oscillations can be excited. For the special case of $\beta = 0$.

$$\Delta_C = 2/N. \tag{66}$$

An important and interesting phenomenon is that the hyperbolic surface $r_0 = (1+\sigma^2)^{\frac{1}{2}}$ puts a cap on the magnitude of the purely radial breathing mode. An alternative way to visualize this is by fixing the forcing frequency and plotting the responses of the two modes as functions of Δ_0. This is shown in figure 5(*a*, *b*). Figure 5(*a*) is a typical bifurcation diagram for fixed σ lying on the interval (σ_L, σ_R). For small forcing amplitude, the response of the breathing mode increases in proportion to the increase of the forcing amplitude. However, after the maximum is reached, the breathing mode becomes unstable through a supercritical pitchfork bifurcation. Afterwards, the response of the radial mode becomes *independent* of the forcing amplitude. The extra energy due to the increased forcing amplitude is transferred

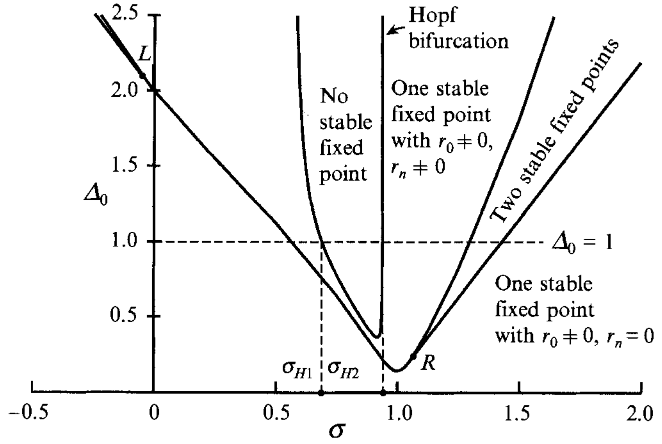

FIGURE 6. Bifurcation sets in the parameter space (σ, Δ_0), for $\beta = 2$.

completely to the shape mode. Figure 5(*b*) is a typical bifurcation diagram for σ lying on the interval (σ_R, ∞) or $(-\infty, \sigma_L)$ of figure 3. In contrast to the previous case, the breathing mode loses stability through a subcritical pitchfork bifurcation, but again the amplitude of radial oscillations is bounded by the surface $r_0 = (1+\sigma^2)^{\frac{1}{2}}$, which is flat in this figure since σ is a constant.

As we pointed out earlier, there is no Hopf bifurcation for $\beta < \beta_c$. Hence, we have seen that there is at least one stable fixed point for all parameters for $\beta = 0$. The bubble undergoes oscillations of constant amplitude for any fixed pair (Δ_0, σ), with a well-defined condition for instability of the purely radial mode, in terms either of the forcing amplitude Δ_0 for fixed σ, or the detuning parameter σ for fixed forcing.

Since nonlinear systems may have more than one attractor, merely following one branch of solutions may not detect attractors in a different part of the phase space. We have therefore done numerical integrations for a large number of initial conditions for fixed parameters. Obviously, using this method, we cannot guarantee that all attractors will be found; nevertheless, the probability of attractors being undetected is small since we have tested a large number of initial conditions. Furthermore, we show in the Appendix that the attractor is contained within a finite hypersphere

$$x_0^2+y_0^2+x_n^2+y_n^2 = (\tfrac{1}{2}\Delta_0)^2/N.$$

Hence we only need to search within the above hypersphere.

Using numerical integration, we have not been able to find chaos for the case of $\beta = 0$. This is illustrative of the fundamental difference that usually exists between a damped and an undamped system (cf. Kovacic & Wiggins 1992). Recall that based on our previous work (Feng & Leal 1993), the modal amplitude equations for free oscillation in an inviscid fluid always have homoclinic orbits when $\beta = 0$, hence any periodic pressure perturbation would have led to chaotic oscillation of the bubble. However, the presence of damping in the current case has changed the outcome completely.

5.2. $\beta = 2$

Let us now consider the case $\beta = 2$ with $N = 20$ $(n = 2)$. Since $\beta > \beta_c$ $(\beta_c = 1.29)$, it is not surprising that Hopf bifurcation occurs. Figure 6 shows the bifurcation sets for this case. We see that there is an open set inside which no stable fixed points of the amplitude functions exist. This means that the amplitude functions are always time-dependent in this zone. This physically corresponds to bubble oscillations with an

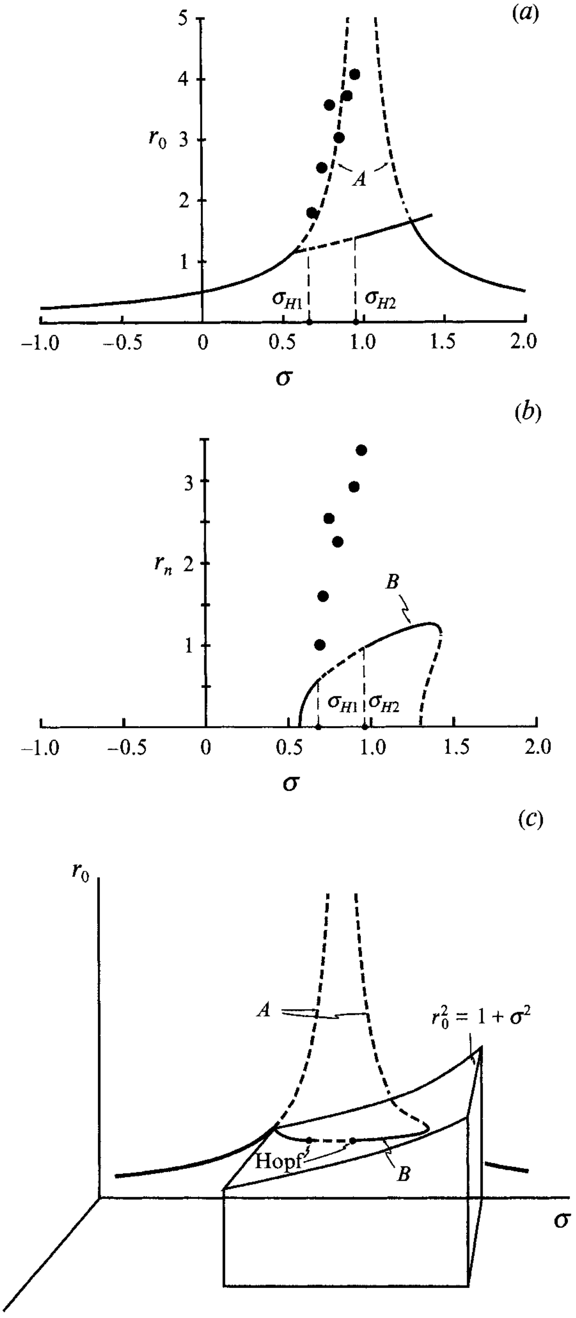

FIGURE 7. Projections into (*a*) (σ, r_0)-space, (*b*) (σ, r_n)-space, and (*c*) schematic perspective in (σ, r_0, r_n)-space of bifurcation diagrams for $\beta = 2$ and $\Delta_0 = 1$. Dots correspond to the maximum values of the time-dependent amplitudes (see §7.3). Solid lines, stable; dashed lines, unstable.

amplitude that is modulated on the slow timescale τ. Note that one of the intersection points in figure 3, point L, is moved upwards and is almost out of the boundary of the figure.

Figure 7 (ignoring the black dots for now, see §7.3) shows the bifurcation diagrams corresponding to a fixed value of Δ_0 ($= 1$). Figures 7(*a*) and 7(*b*) show the projections

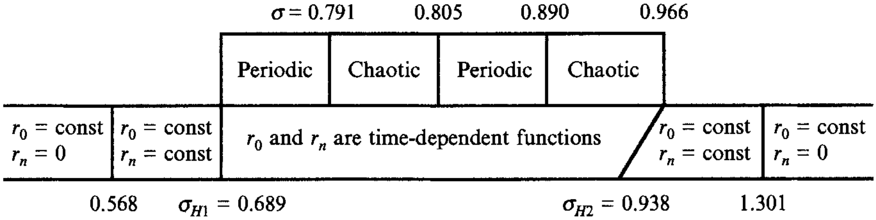

FIGURE 8. Overall dynamics of the bubble for $\Delta_0 = 1$, $\Delta_n = 0$, $\beta = 2$.

of the bifurcation diagram into (σ, r_0)- and (σ, r_n)-space. Figure 7(*c*) shows the same bifurcation diagram in perspective and is hence easier to visualize. Branches marked *A* and *B* denote fixed-point solutions of the amplitude equations which physically correspond to periodic motions of the bubble. In particular, Branch *A* corresponds to a purely radial response and Branch *B* corresponds to both radial and shape oscillations. The solid-line segments of the two branches denote stable regimes while the dashed-line segments denote unstable regimes. Since this bifurcation diagram is obtained for $\Delta_0 = 1$, the σ-values at which bifurcation occurs can be obtained by taking a horizontal cut of the bifurcation sets in figure 6. As noted above, there is an open interval, $(\sigma_{H1}, \sigma_{H2})$, where $\sigma_{H1} = 0.689$ and $\sigma_{H2} = 0.938$, on which no stable fixed point exists for the amplitude functions r_0 and r_n.

At the two Hopf bifurcation points σ_{H1} and σ_{H2}, two new branches of periodic solutions come into existence. It is useful to know how these two branches of periodic solutions evolve as the parameter σ is varied. The program AUTO for continuation and bifurcation problems in ordinary differential equations by Doedel (1986) is best suited for investigating this point. Given the coordinates of the fixed points for a particular value of σ as starting points, the program automatically traces out the fixed point for all values of σ in a given interval. At the same time, the program calculates the stability of the fixed point and locates bifurcation points on the solution branch. It can automatically switch to new branches bifurcating from the previous solution branches. Furthermore, AUTO allows us to follow the periodic solutions, which come into existence at the Hopf bifurcations, and to study the stability and bifurcation of these solutions as σ varies. Denote the branches of periodic solutions generated at σ_{H1} and σ_{H2} as branch 1 and 2. Using AUTO, we find for branch 1 that periodic solutions exist for σ on the interval $(\sigma_{H1}, 0.966)$. At $\sigma = \sigma_{H1}$ the periodic solution coincides with the fixed point. As σ increases, the amplitude of the periodic solution increases. At $\sigma = 0.966$, the amplitude of the periodic solution has grown such that it nearly hits the unstable fixed point $r_0 = \text{constant}$ and $r_n = \text{constant}$. When this occurs the period of the periodic solution becomes very large, indicating that the periodic solutions terminate at a homoclinic orbit. The Floquet multipliers of the periodic solution calculated by AUTO also show that the periodic solution near σ_{H1} is stable. The stability is soon lost at $\sigma = 0.786$ through a period-doubling bifurcation. For branch 2, periodic solutions are found to exist for σ on the interval $(\sigma_{H2}, 1.000)$. These terminate at $\sigma = 1.000$ where the periodic solution coincides with a homoclinic orbit that connects the unstable fixed point $r_0 = \text{constant}$ and $r_n = 0$ to itself. The branch-2 periodic solutions are unstable for all possible values of σ.

In order to study the nature of the attractors for σ on the interval of $(\sigma_{H1}, \sigma_{H2})$, we again numerically integrate system (44) for a large number of initial conditions. Figure 8 summarizes the nature of time-dependent attractors for a range of σ-values. The attractors we found are periodic except for σ between 0.791 and 0.805 and for σ

between 0.890 and σ_{H2}, where they are chaotic. In fact the latter interval of chaos extends beyond σ_{H2} to $\sigma = 0.960$ so that for σ between σ_{H2} and 0.960, both fixed-point attractors and chaotic attractors are possible. In figure 9, we plot numerically calculated projections of the phase diagrams into (r_0, r_n)-space for various values of σ on this interval and for $\Delta_0 = 1$, $\beta = 2$. The transition from a stable fixed point at $\sigma = 0.65$ through regions of periodic and chaotic attractors with increase of σ is clearly visible, until finally another stable fixed point is achieved at $\sigma = 1$.

Before we conclude our study of this case, we note that no chaos is found to occur when either $\sigma = 0$, or $\sigma = \frac{1}{2}\beta$, both of which correspond to cases of exact external resonances ($\Omega = \omega_n$ and $2\Omega = \omega_0$ respectively).

5.3. $\beta = 1$

Since β is less than β_c (1.29), this case is qualitatively similar to $\beta = 0$ except that the symmetry is distorted. It is not difficult for the reader to imagine the bifurcation sequences. Again at least one steady state exists for all possible parameter values. No time-dependent attractors are found. The bifurcation sets are shown in figure 10.

We shall discuss some additional conclusions of the preceding analysis in §7. First, however, we consider the case of anisotropic pressure forcing, with $\Delta_n \neq 0$ but $\Delta_0 = 0$.

6. Dynamics of a bubble forced by an anistropic pressure distribution, $\Delta_0 = 0$

Again we start the bifurcation analysis by identifying the fixed points. The fixed points can be found by the following steps. Solving (43*a*) and (43*b*) for r_0 and $(2\theta_n - \theta_0)$, we get

$$r_0^2 = \frac{r_n^4}{4/N^2 + (\beta - 2\sigma)^2}, \quad \tan(2\theta_n - \theta_n) = -\frac{2}{N(\beta - 2\sigma)}. \qquad (67\,a, b)$$

Substituting these results into (43*c*) and (43*d*), and eliminating θ_n, we obtain

$$r_n^6 + \left[\frac{4}{N} - 2\sigma(\beta - 2\sigma)\right] r_n^4 + (1 + \sigma^2)\left[\frac{4}{N^2} + (\beta - 2\sigma)^2\right] r_n^2 - \left[\frac{4}{N^2} + (\beta - 2\sigma)^2\right] \Delta_n^2 = 0. \quad (68)$$

Equation (68) can be used to solve for the amplitude of the shape mode at fixed points of the system (41). Once r_n is known, it can be substituted into (67*a*) to obtain the corresponding amplitude of the breathing mode. For fixed N-, Δ_n- and β-values, we can also obtain the bifurcation diagram, r_n versus σ, by plotting the level curves of (68). If we substitute r_0 for r_n by using (67*a*), we can also obtain the bifurcation diagram, r_0 versus σ.

A stability analysis of the above fixed points could be pursued in the same manner as for the isotropically forced case. However, owing to the complicated form of the roots of the cubic equation (68), a numerical method provides a simpler approach. The program AUTO is again used.

The bifurcation sets obtained using AUTO for $\beta = 0$ are presented in figure 11. The parabolic shaped curve in this figure corresponds to the σ- and Δ_n-values at which Hopf bifurcation occurs. Inside the curve, there is no time-independent stable fixed point. In this zone, the two amplitude functions, α_0 and α_n, of the volume and shape modes are time modulated. This time modulation may be periodic on a slow timescale or it may be chaotic. In addition to the curve corresponding to the Hopf bifurcation,

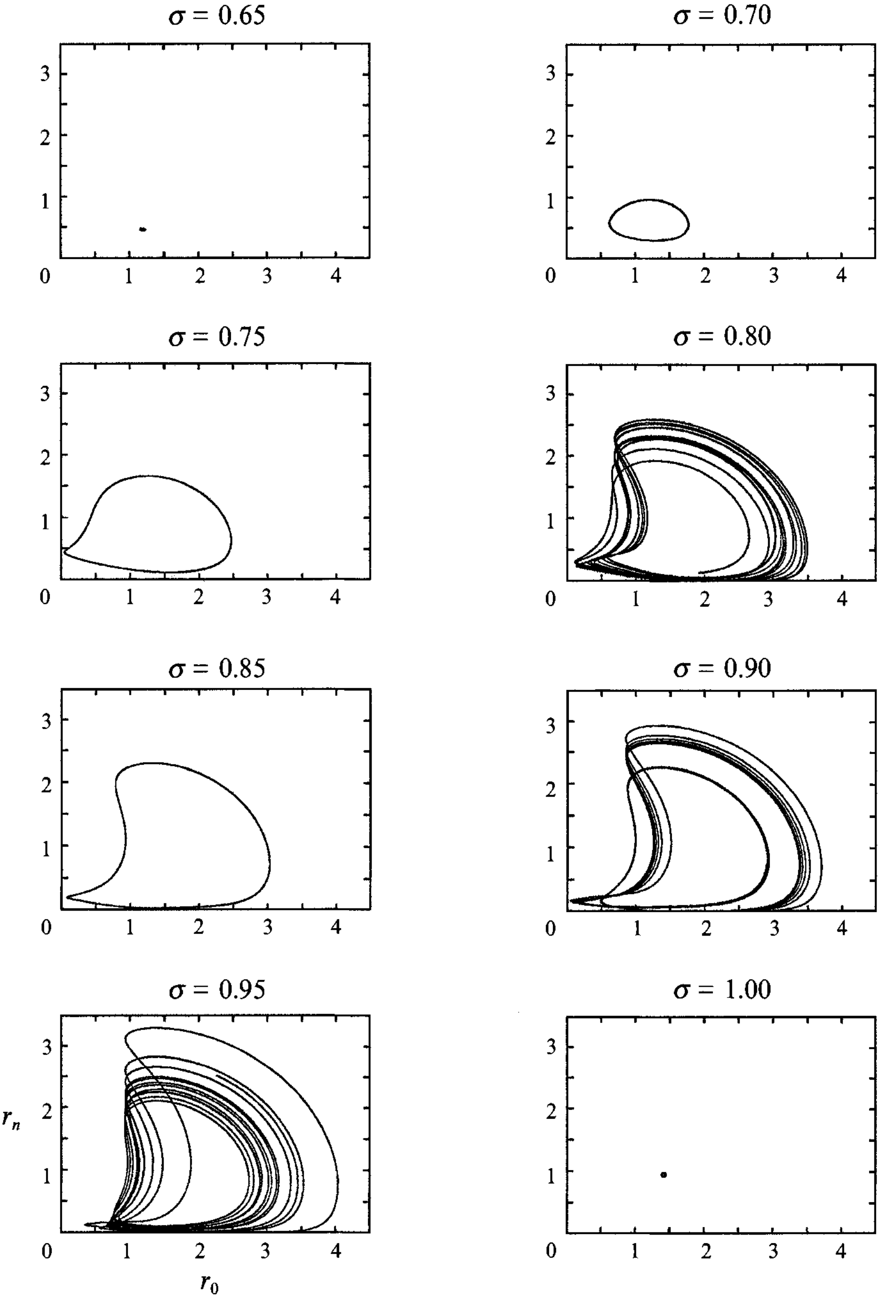
σ = 0.65
σ = 0.70
σ = 0.75
σ = 0.80
σ = 0.85
σ = 0.90
σ = 0.95
σ = 1.00

FIGURE 9. Projections of phase diagrams into (r_0, r_n)-space for various values of σ which lie in the interval of figure 7 for which no stable states exist.

there are two needle-shaped curves which correspond to a saddle-node bifurcation. Inside these curves, there are two stable fixed points, both of which involve volume and shape modes of constant amplitude. However, one fixed point corresponds to volume and shape oscillations of significantly larger amplitude than the other; this will be seen clearly later in figure 12. In experiments where the forcing amplitude (or the frequency) is slowly changed, the transitions from one fixed point to the other will depend on

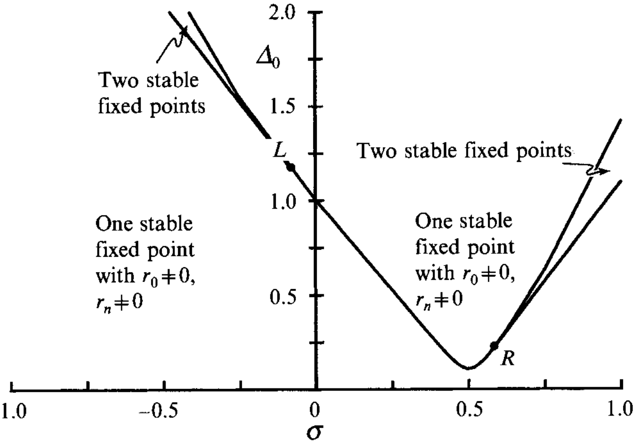

FIGURE 10. Bifurcation sets in (σ, Δ_0)-space for fixed $\beta = 1.0$. No Hopf bifurcation occurs.

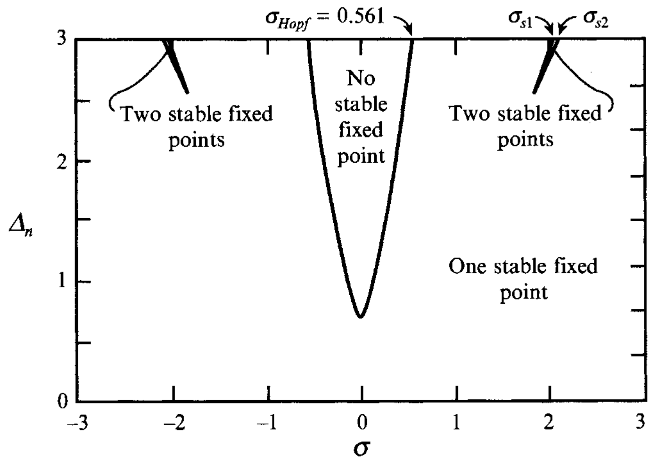

FIGURE 11. Bifurcation sets in (σ, Δ_n)-space for fixed $\beta = 0$.

whether we are increasing or decreasing the forcing amplitude (or frequency). For parameters outside the above three curves, there is only one stable fixed point.

To understand the bifurcation sequences, we take a horizontal cut of figure 11 and plot the bifurcation diagram for fixed $\Delta_n = 3$. The projections of the bifurcation diagram in (σ, r_0)-space and (σ, r_n)-space are shown in figure 12(*a*) and 12(*b*) respectively. For large positive σ, corresponding to high-frequency forcing, the amplitude of the breathing mode is very small. However, as σ decreases below σ_{s1}, a saddle-node bifurcation occurs. The amplitudes of both the breathing mode and the shape mode jump to a larger value. As σ further decreases, the amplitude of the breathing mode remains more or less the same while the amplitude of the shape mode decreases monotonically, which is typical of systems with quadratic nonlinearity for which responses of maximum amplitude occur away from exact resonance. As σ gets closer to zero, the stable steady state becomes unstable through a Hopf bifurcation at σ_{Hopf}, where $\sigma_{Hopf} = 0.561$. Within the interval of σ in $(0, \sigma_{Hopf})$, there are only time-dependent attractors, which are found to be either periodic or chaotic depending on the exact value of σ. In this region, the amplitude functions for both the volume mode and the shape mode are either periodic or chaotic functions of the slow time variable, τ.

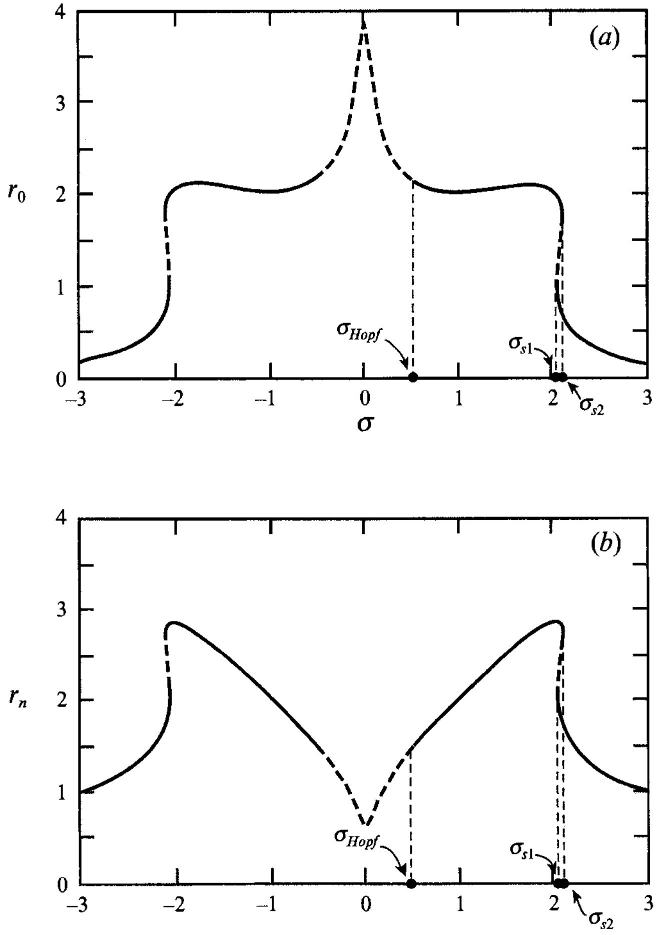

FIGURE 12. Projections of bifurcation diagrams into (*a*) (σ, r_0)-space and (*b*) (σ, r_n)-space for $\beta = 0$ and $\Delta_n = 3$. Solid lines, stable; dashed lines, unstable.

Calculation by AUTO shows that a branch of periodic solutions connects the two Hopf bifurcation points at $\sigma = -\sigma_{Hopf}$ and $\sigma = \sigma_{Hopf}$. Focusing on the positive half of the interval, at σ_{Hopf}, a supercritical bifurcation occurs leading to stable periodic orbits for σ slightly less than σ_{Hopf}. As σ further decreases, this branch of periodic orbits soon loses stability through a period-doubling bifurcation at $\sigma = 0.523$. This now unstable branch regains stability through a saddle-node type of bifurcation (of periodic orbits) at $\sigma = 0.118$. It remains stable until $\sigma = 0$. The behaviour of the periodic orbits on the other half of the interval can be obtained by symmetry. Conceivably, the period-doubling bifurcation at $\sigma = 0.523$ is followed by a period-doubling cascade which accumulates at $\sigma = 0.515$ so chaos occurs for σ just smaller than $\sigma = 0.515$. It appears that the loss of stability of the periodic orbit for σ slightly greater than $\sigma = 0.118$ marks one end of the interval of chaos. An investigation of the cause of the transition between periodic and chaotic motions at $\sigma = 0.225$ and $\sigma = 0.458$ is beyond the scope of this paper.

Merely following the periodic solutions bifurcating at the Hopf bifurcation points will not detect time-dependent attractors that are not connected to the above periodic solutions through bifurcations. Hence we use numerical integration to study the time-

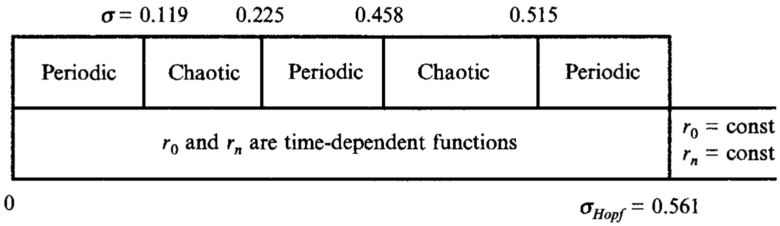

FIGURE 13. Overall dynamics of the bubble for $\Delta_0 = 0$, $\Delta_n = 3$, $\beta = 0$.

dependent attractors for various values of σ on the interval $(0, \sigma_{Hopf})$ in a similar manner as for the isotropically forced case. We find that the attractors are periodic except for σ on the intervals of (0.119, 0.225) and (0.458, 0.515) as shown in figure 13. In figure 14, we plot numerically calculated projections of the attractors into (r_0, r_n)-space for various values of σ on the interval $(0, \sigma_{Hopf})$. The transition from a stable fixed point at $\sigma = 0.6$ through a series of periodic and chaotic solutions as σ is decreased to 0 is clearly visible.

We note that for the anisotropically forced case, although chaos can indeed occur for $\beta = 0$ as we might have expected from our previous work (Feng & Leal 1993), the occurrence of chaos is dependent on the forcing frequency.

The bifurcation sets for $\beta = 2.0$ as shown in figure 15. Note that the symmetry of figure 11 is destroyed, but other than that, there is no significant difference between these two figures.

7. Physical interpretation

In the following, we discuss the physical interpretation of several of the results obtained in the previous two sections. In particular we analyse the stability of a pulsating spherical bubble, the effect of frequency detuning and the consequences of chaotic bubble oscillations. We note that since the assumptions leading to the amplitude equations are just scaling assumptions, our amplitude equations are valid even when they yield chaotic solutions.

7.1. *Stability of a pulsating spherical bubble*

Equation (52) gives the criterion for stability of a pulsating spherical bubble. Although it is obtained from a general analysis of (41), whose derivation in §3 is based on the assumption that the forcing frequency is close to the natural frequency of the volume mode, we know from the discussion in §4, that the stability criterion is equally valid for forcing frequencies that are not near the resonance frequency of the volume mode. From our earlier discussion, it is also evident that the stability criterion for a pulsating spherical bubble is applicable to both an ideal gas bubble and an isothermal vapour bubble.

Substituting (40) and (42) into (52), we obtain

$$|\alpha_{1,0}| < \frac{1}{H_6}[(N\tilde{S})^2 + \sigma_n^2]^{\frac{1}{2}}. \tag{69}$$

Multiplying both sides of (69) by ϵ and substituting (18) and (16) into it, we have

$$|f| < \frac{1}{H_6}[(NS)^2 + (\Omega - \omega_n)^2]^{\frac{1}{2}}.$$

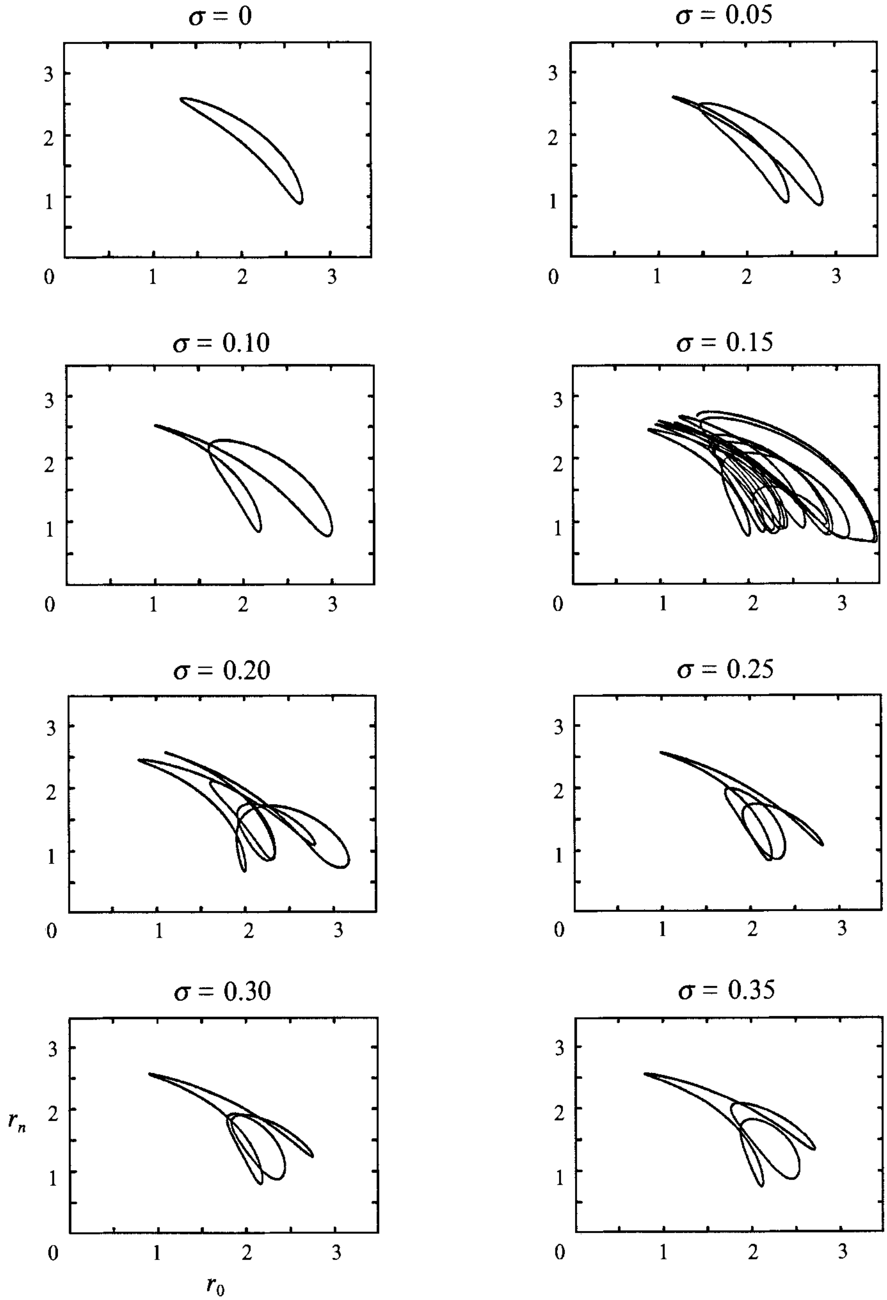
$\sigma = 0$, $\sigma = 0.05$, $\sigma = 0.10$, $\sigma = 0.15$, $\sigma = 0.20$, $\sigma = 0.25$, $\sigma = 0.30$, $\sigma = 0.35$

FIGURE 14. For caption see facing page.

Finally recalling (38) and (39), we can express the stability criterion in the following form:

$$|f| < \frac{2}{(4n-1)\,\omega_n}[(2(2n+1)(n+2)\,S)^2 + (2\Omega - 2\omega_n)^2]^{\frac{1}{2}}. \tag{70}$$

When the viscous effect is ignored, (70) is identical to the stability criterion obtained by Feng & Leal (1993). Note however that the oscillation frequency of the breathing

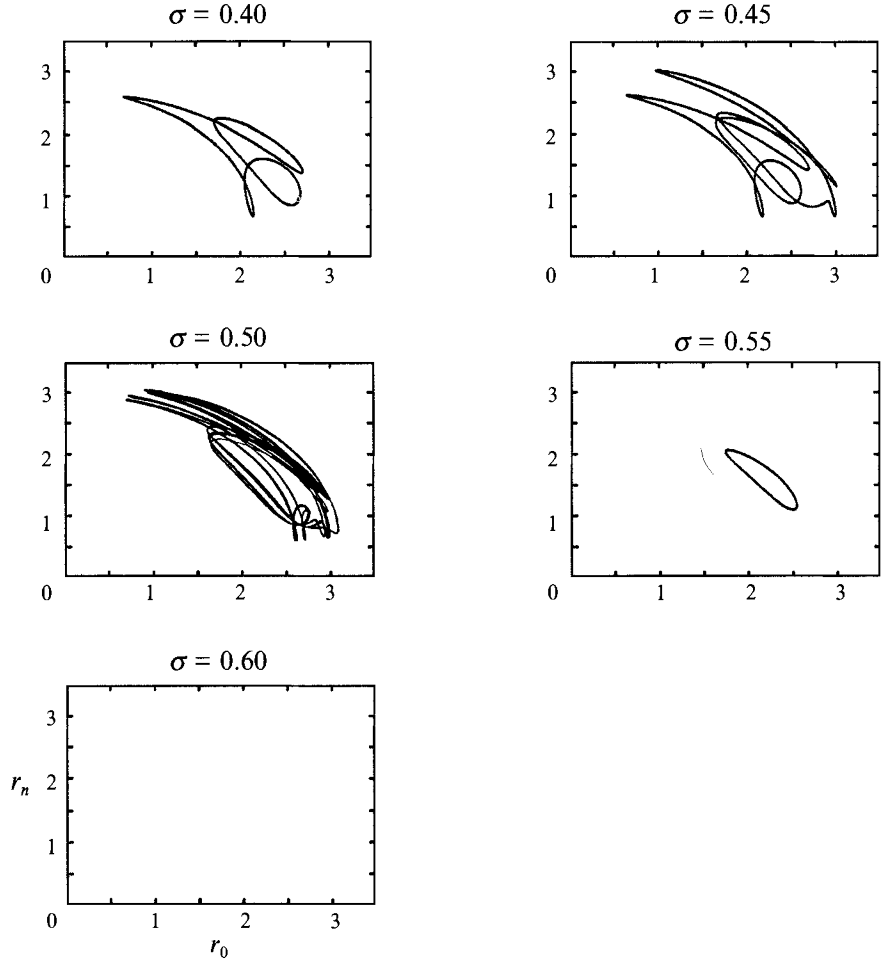

FIGURE 14. Projection of phase diagrams into (r_0, r_n)-space for various values of σ which lie in the interval of figure 12 for which no stable steady states exist.

mode is 2Ω. The stability boundary defined by (70) is shown in figure 16. The stability boundary for inviscid fluids is also given (dashed lines). In our previous work (Feng & Leal 1993), we pointed out that the stable region for higher modes is smaller than that for the lower modes. From figure 16, we conclude that the same is true here. The higher modes, though having much higher dissipation, are still less stable than the lower modes. The implication is that a bubble oscillating at higher frequency is less stable than the same bubble oscillating at lower frequency. The result is not too surprising when we recall that the kinetic energy of a pulsating bubble is proportional to the square of the frequency and it is reasonable to assume that a bubble with more energy is less stable. The larger dissipation of the higher modes is not sufficient to counterbalance the increased kinetic energy associated with higher oscillation frequency.

7.2. *Effect of frequency detuning*

In the isotropically forced case, chaos is found to occur only for $\beta > \beta_c$, and on an interval of σ which lies between $\frac{1}{4}\beta$ and $\frac{1}{2}\beta$. We know that when $\beta = 0$ exact internal resonance occurs, and that when $\sigma = 0$ or $\sigma = \frac{1}{2}\beta$ exact resonance between the shape

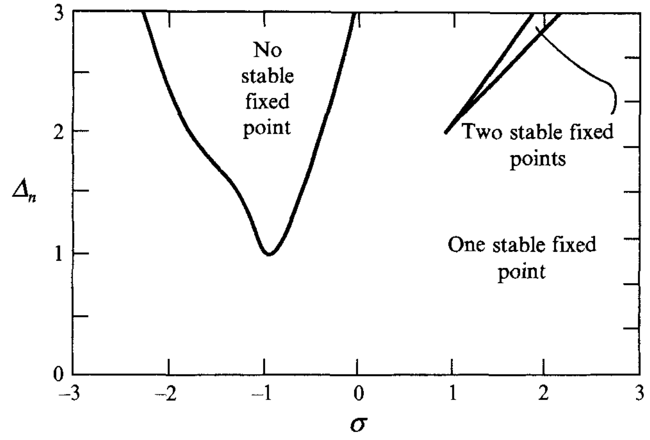

FIGURE 15. Bifurcation sets in (σ, Δ_n)-space for fixed $\beta = 2$.

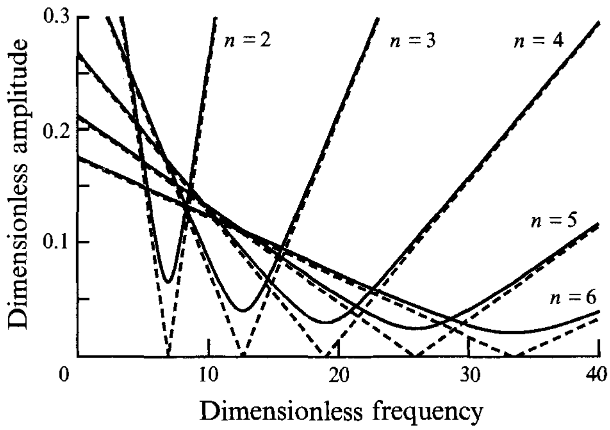

FIGURE 16. Stability boundaries for resonances between volume mode and various shape modes. Solid lines, $S = 0.01$; dashed lines, $S = 0$.

mode or the volume mode and the forcing occurs. In none of these exact resonance cases do we find chaos. This is not true for the anisotropically forced case. We have shown that chaos occurs in this case even for exact internal resonance conditions.

7.3. *Consequences of chaotic bubble oscillations*

In figure 17, we show the power spectra of r_0 for two of the cases shown in figure 9, as determined through a fast-Fourier-transform program given in Miles (1984*a*). In the first case, $\sigma = 0.70$, where there is a periodic attractor as shown in figure 9, the power spectra shown in figure 17(*a*) consists of a large peak at the frequency of periodicity as well as its higher harmonics. When the attractor is chaotic however (at $\sigma = 0.95$), we observe a broadband power spectrum. Since r_0 is associated with changes of the bubble volume, when chaotic attractors arise in our amplitude equation, we expect any sound produced by oscillations of bubble volume to have a similarly broadband power spectra.

In addition, chaos also results in dramatic effects on the oscillation amplitudes. This is clearly shown in figure 7, where the dots indicate peak amplitudes of both the volume mode and the shape mode; recall that on the interval $\sigma_{H1} < \sigma < \sigma_{H2}$, there are no

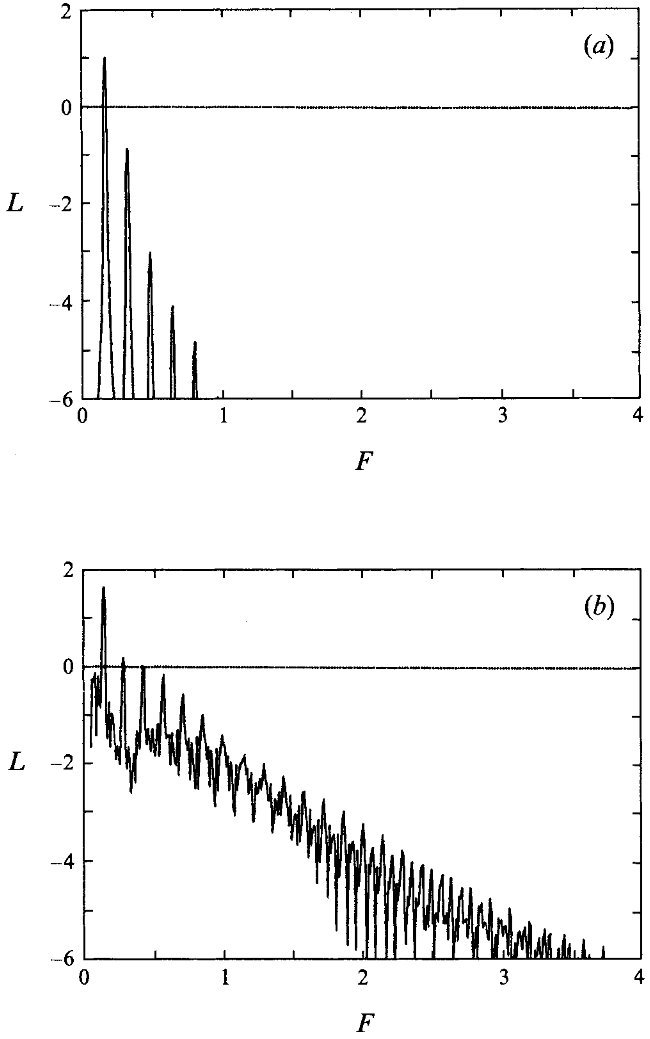

FIGURE 17. Power spectra of r_0 for (*a*) $\sigma = 0.70$, (*b*) $\sigma = 0.95$. F and L are defined as in Miles (1984*a*).

stable fixed points. Note that the peak amplitudes are about three to four times larger than the largest amplitudes of the steady state. Interestingly the peak amplitude of the volume mode is very close to the amplitude that would occur for the volume mode if no shape deformation were allowed (dashed curves of figure 7*a*).

In many physical applications, it is the peak amplitude that is of relevance. For example, when the peak amplitude of the shape mode exceeds a certain value, it may suggest that the shear stress in the fluid has exceeded a threshold value or that the bubble is breaking.

We also observe from figure 7(*b*) that as we decrease the forcing frequency, the transition from regular motions to chaotic motions is not continuous. At σ roughly equal to 1, we see stable oscillations of both the volume mode and the shape mode. However, as σ is decreased a little bit further, we encounter a catastrophic phenomenon where the bubble oscillation changes from regular to chaotic with only a very slight change of the forcing frequency.

One primary objective of this work was to provide a framework to guide corresponding experimental studies. Since all of the different types of attractors discovered above occur on a narrow frequency interval due to the near-resonance conditions (15) and (16), a detailed study of the chaotic attractors is not given. For instance, though it is possible, using numerical means, to identify period-doubling bifurcation sequences which lead to chaotic motions from regular motions, such a result, in our opinion, would not be very useful in a real experiment because of the demand on the frequency resolution of the instrument. The result that we believe is most useful in guiding experiments is the bifurcation diagrams we obtained. Through these bifurcation diagrams, we illustrated the sequences of transition between periodic, quasi-periodic and chaotic bubble oscillations. In actual experiments, though we cannot expect accurate quantitative agreement with the theory, qualitative agreement, specifically the sequences of transitions, is expected. Furthermore, for the isotropically forced case, we have identified a critical internal frequency detuning β_c below which chaotic bubble oscillation has not been observed.

This work was supported primarily by a grant from the Fluid Mechanics program of the ONR. We also acknowledge partial support by NASA through the Microgravity Science Program. Suggestions and criticisms from the referees are appreciated.

Appendix. Asymptotic properties of the amplitude equations (44)

To make our analysis slightly more general, we consider the following dynamical system:

$$\begin{aligned}\dot{x}_0 &= -d_1 x_0-(\beta-2\sigma)y_0-2x_n y_n,\\ \dot{y}_0 &= (\beta-2\sigma)x_0-d_1 y_0+x_n^2-y_n^2+\Delta_0,\\ \dot{x}_n &= -d_2 x_n+\sigma y_n-(y_0 x_n-x_0 y_n),\\ \dot{y}_n &= -\sigma x_n-d_2 y_n+x_0 x_n+y_0 y_n+\Delta_n,\end{aligned}$$

where an over-dot corresponds to differentiation with respect to a time-like variable τ. If $d_1 = 2/N$ and $d_2 = 1$, (44) is recovered. We also assume that $d_2 > d_1 > 0$, which is the case we are interested in since $N > 2$. Let

$$R^2 = x_0^2+y_0^2+x_n^2+y_n^2.$$

Differentiate R^2 with respect to τ. Substituting the above differential equations for $\dot{x}_0$, $\dot{y}_0$, etc. we obtain

$$R\dot{R} = -d_1(x_0^2+y_0^2)-d_2(x_n^2+y_n^2)+\Delta_0 y_0+\Delta_n y_n,$$

i.e.
$$R\dot{R} = \frac{d_1}{2}\left[-2(x_0^2+y_0^2)-\frac{2d_2}{d_1}(x_n^2+y_n^2)+2\frac{\Delta_0}{d_1}y_0+2\frac{\Delta_n}{d_1}y_n\right].$$

Using
$$2\frac{\Delta_0}{d_1}y_0+2\frac{\Delta_n}{d_1}y_n \leqslant \left(\frac{\Delta_0}{d_1}\right)^2+\left(\frac{\Delta_n}{d_1}\right)^2+y_0^2+y_n^2,$$

we get

$$\begin{aligned}R\dot{R} &\leqslant \frac{d_1}{2}\left[\left(\frac{\Delta_0}{d_1}\right)^2+\left(\frac{\Delta_n}{d_1}\right)^2-(x_0^2+y_0^2+x_n^2+y_n^2)-x_0^2-\left(\frac{2d_2}{d_1}-1\right)x_n^2-\left(\frac{2d_2}{d_1}-2\right)y_n^2\right]\\ &\leqslant \frac{d_1}{2}[R_0^2-R^2],\end{aligned}$$

where $$R_0^2 = \left(\frac{\varDelta_0}{d_1}\right)^2 + \left(\frac{\varDelta_n}{d_1}\right)^2.$$

The last step follows from the fact that $d_2 > d_1 > 0$. Thus we see that for all $R \geqslant R_0$, $\dot{R} \leqslant 0$. Therefore, all attractors of the dynamical system must lie within a hypersphere of radius R_0. The radius of the hypersphere, for the special cases of either $\varDelta_0 = 0$ or $\varDelta_n = 0$, is proportional to the forcing amplitude and inversely proportional to the damping coefficient of the weaker one.

REFERENCES

BENJAMIN, T. B. & ELLIS, A. T. 1990 Self-propulsion of asymmetrically vibrating bubbles. *J. Fluid Mech.* **212**, 65–80.

CRUM, L. A. & PROSPERETTI, A. 1983 Nonlinear oscillations of gas bubbles in liquids: an interpretation of some experimental results. *J. Acoust. Soc. Am.* **73**, 121–127.

DOEDEL, E. 1986 *AUTO: Software for Continuation and Bifurcation Problems in Ordinary Differential Equations.* California Institute of Technology.

FENG, Z. C. & LEAL, L. G. 1993 Energy transfer mechanism in coupled bubble oscillations. *Phys. Fluid* A **5**, 826–836.

FFOWCS WILLIAMS, J. E. & GUO, Y. P. 1991 On resonant nonlinear bubble oscillations. *J. Fluid Mech.* **224**, 507–529.

GUCKENHEIMER, J. & HOLMES, P. 1983 *Nonlinear Oscillations, Dynamical Systems, and Bifurcations of Vector Fields.* Springer.

HOLT, R. G. & CRUM, L. A. 1992 Acoustically forced oscillations of air bubbles in water: experimental results. *J. Acoust. Soc. Am.* **91**, 1924–1932.

JOSEPH, D. D. 1973 Domain perturbations: the higher order theory of infinitesimal water waves. *Arch. Rat. Mech. Anal.* **51**, 295–303.

KANG, I. S. & LEAL, L. G. 1988 Small-amplitude perturbations of shape for a nearly spherical bubble in an inviscid straining flow (steady shapes and oscillatory motion). *J. Fluid Mech.* **187**, 231–266.

KOVACIC, G. & WIGGINS, S. 1992 Orbits homoclinic to resonances, with an application to chaos in a model of the forced and damped Sine-Gordon equation. *Physica* D **57**, 185–225.

LAMB, H. 1932 *Hydrodynamics*, 6th edn. Cambridge University Press (Dover edn 1945).

LAUTERBORN, W. & PARLITZ, U. 1988 Methods of chaos physics and their application to acoustics. *J. Acoust. Soc. Am.* **84**, 1975–1993.

LONGUET-HIGGINS, M. S. 1989 Monopole emission of sound by asymmetric bubble oscillations. Part 2. An initial value problem. *J. Fluid Mech.* **201**, 543–565.

LONGUET-HIGGINS, M. S. 1991 Resonance in nonlinear bubble oscillations. *J. Fluid Mech.* **224**, 531–549.

MARSTON, P. L. & APFEL, R. E. 1980 Quadrupole resonance of drops driven by modulated acoustic radiation pressure – Experimental properties. *J. Acoust. Soc. Am*, **67**, 27–37.

MEI, C. C. & ZHOU, X. 1991 Parametric resonance of a spherical bubble. *J. Fluid Mech.* **229**, 29–50.

MILES, J. 1984*a* Resonant motion of a spherical pendulum. *Physica* **11D**, 309–323.

MILES, J. 1984*b* Resonantly forced motion of two quadratically coupled oscillators. *Physcia* **13D**, 247–260.

NAYFEH, A. H. & MOOK, D. T. 1979 *Nonlinear Oscillations.* Wiley.

PARLITZ, U., ENGLISCH, V., SCHEFFCZYK, C. & LAUTERBORN, W. 1990 Bifurcation structure of bubble oscillators. *J. Acoust. Soc. Am.* **88**, 1061–1077.

PLESSET, M. S. & PROSPERETTI, A. 1977 Bubble dynamics and cavitation. *Ann. Rev. Fluid Mech.* **9**, 145–185.

PROSPERETTI, A. 1977 Viscous effects on perturbed spherical flows. *Q. Appl. Maths* **34**, 339–352.

SETHNA, P. R. 1965 Vibrations of dynamical systems with quadratic nonlinearities. *Trans. ASME J. Appl. Mech.*, Sept., 576–582.

SMEREKA, P., BIRNIR, B. & BANERJEE, S. 1987 Regular and chaotic bubble oscillations in periodically driven pressure fields. *Phys. Fluids* **30**, 3342–3350.

STRASBERG, M. & BENJAMIN, T. B. 1958 Excitation of oscillations in the shape of pulsating bubbles – experimental work. *J. Acoust. Soc. Am.* **30**, 697 (A).

SZERI, A. & LEAL, L. G. 1991 The onset of chaotic oscillations and rapid growth of a spherical bubble at subcritical conditions in an incompressible liquid. *Phys. Fluids* A **3**, 551–555.

WIGGINS, S. 1988 *Global Bifurcation and Chaos – Analytical Methods.* Springer.

YANG, S. M., FENG, Z. C. & LEAL, L. G. 1993 Nonlinear effects in dynamics of shape and volume oscillation for a gas bubble in an external flow. *J. Fluid Mech.* **247**, 417–454.

YOUNG, F. R. 1989 *Cavitation.* McGraw-Hill.